Spatially evolving regular water wave under the action of steady wind forcing

Lev Shemer* and Santosh Kumar Singh
School of Mechanical Engineering, Tel-Aviv University, Tel-Aviv 69978, Israel

(Received 15 December 2020; accepted 3 March 2021; published 19 March 2021)

Detailed investigation of spatial evolution of mechanically generated regular water waves in a wind-wave tank under the action of steady wind is carried out. Deterministic waves are excited by a wavemaker driven at a range of frequencies and wavemaker displacement amplitudes. Prolonged measurements of the temporal variation of the instantaneous surface elevation carried out at multiple locations along the test section at numerous airflow rates enable obtaining reliable statistical parameters characterizing the wave-field evolution. Particular attention is given to the development along the tank of the wave frequency spectra as a result of wind input and interaction of the deterministic mechanical and the random wind waves. The interrelation between the regular and the random parts of the resulting wave field is studied in detail using auto- and cross-covariance analysis. Spatial coherence of the wave field is evaluated as a function of frequency for different wavemaker operation parameters and wind. The accumulated results allow us to draw conclusions regarding the effect of the high-frequency waves at short fetches evolving under the action of wind-wave field at more remote locations.

DOI: 10.1103/PhysRevFluids.6.034802

I. INTRODUCTION

In spite of significant efforts invested during the last hundred years in theoretical and experimental studies of physical processes governing the interaction of atmosphere and ocean in general, and, more specifically, of the growth of water surface waves in time and space in the presence of wind, our understanding of mechanisms governing wind-wave evolution remains incomplete [1]. The inherent complexity of the problem leads to considerable difficulties in accumulating reliable and detailed experimental data that can serve as a basis for wind-wave modeling. Field experiments at natural scales in oceans and lakes are often subjected to unpredictable and uncontrollable environmental conditions that complicate extracting verifiable and accurate information. Moreover, field measurements usually yield limited information on wave evolution with fetch and thus on wind-wave growth rates. Experiments on wind waves in the laboratory allow us to circumvent many of those difficulties and to perform accurate measurements under controlled conditions. However, even in the largest available laboratory installations wind waves are shorter by orders of magnitude than in nature. As a result, waves in the laboratory are necessarily young. Their wave age c_p/u_*, c_p being the celerity of the dominant waves and u_* the friction velocity at the air-water interface, is much smaller than that of ocean waves; waves in the laboratory are usually steeper than in nature, thus nonlinear effects may be more pronounced. The contribution to the spectra of very short waves affected by surface tension is often larger. Additional factors may have a pronounced effect on wind waves in the laboratory as compared to much longer waves in nature [2–4]. The relevance of small-scale laboratory studies to wind waves in nature may be evaluated by carrying out a quantitative comparison of results obtained in wind-wave tanks with those accumulated in

*Corresponding author: shemerl@tauex.tau.ac.il

large-scale field measurements using dimensional analysis [5] in which the friction velocity u_* is used as the velocity scale. Experiments in a large wind-wave facility demonstrated that under steady wind forcing, dimensionless peak spectral frequency and dimensionless characteristic wave amplitudes depend on the dimensionless fetch according to a power law [6,7]. Measurements in our facility [8] yielded results consistent with [6,7]. Note that the generally adopted scaling for spatial evolution of the characteristic wind-wave parameters [9,10] does not contain the wave age c_p/u_* explicitly. Detailed measurements of spatially evolving wind waves under steady wind forcing carried out for a wide range of wind velocities in our moderately sized experimental facility demonstrated that wave power spectra measured at different fetches and wind velocities, when properly normalized, collapse on a single Joint North Sea Wave Observation Project (JONSWAP) spectral shape that characterizes wave spectra in the sea.

Waves in natural reservoirs are often excited by wind over already existing wave systems that were initially generated by remote storms (the swell). The interaction of the evolving young wind waves with the existing waves is therefore of considerable interest. In an early experimental work on wind waves propagating over a monochromatic wave train in a laboratory wave tank, Mitsuyasu [11] observed the suppression of wind waves depending on the long wave steepness. Similar suppression of short wind waves was also observed in experiments by Phillips and Banner [12] who explained it theoretically by considering the effect of the drift induced by the orbital velocity of the steep long wave on the short wind waves. Later, Donelan [13] suggested a different mechanism for suppression of wind waves, in which the long waves disrupt the nonlinear interactions among the wind waves thus reducing the energy in the high-frequency part of the spectrum.

Chen and Belcher [14] formulated a quantitative theoretical model that explains the suppression of the short wind waves by a sheltering mechanism which reduces the turbulent wind shear stress for generation of those waves. The model results were found to be in general agreement with experiments [11–13]. Recently, Bailey *et al.* [15] investigated experimentally the applicability of the wind-wave suppression model [14] to irregular long waves and showed that it accurately predicts the reduction of the wind waves energy density in the presence of long waves as a function of wave steepness but underestimates the short wind-wave dissipation.

The effect of wind on Benjamin-Feir instability of a nonlinear wavemaker generated wave train in a large wind-wave tank was examined in [16]. Coupling of wind and mechanically generated waves in a tank was investigated and compared with the theoretical model in [17], while the effect of nonlinear coupling due to resonant interactions was studied numerically in bimodal spectra in deep water waves in [18]. The nonlinear coupling between swell and wind sea has been shown to cause swell growth at the expense of the wind sea in the frequency range just below the peak frequency of the wind sea. Results presented in [19,20] indicate that the spectral changes are mainly controlled by nonlinearity, while wind input and dissipation play a relatively minor role.

Numerous studies were conducted in which the effect of a deterministic wave under steady wind on velocity fields in air and water was investigated (see Refs. [21,22] and additional references therein). Those studies provide detailed information on the flow field in the vicinity of air-water interface, including the distribution of stresses and the wave energy budget. They report on velocity and stress distributions in air and water and thus contribute significantly to understanding of physical mechanisms of momentum and energy transfer from wind to waves and thus allow estimates of wave field evolution under the action of wind under various operational conditions [23]. However, the issue of wind effect on the deterministic wave itself is often not addressed; moreover, those studies are predominantly carried out at a single location and thus do not provide direct information on variation of the governing wave parameters with fetch. Attempts to simulate the interaction of sea swell with wind waves in the laboratory [24–26] demonstrated a dramatic modification of the wavemaker-generated water wave by the wind-excited waves. Measurements of the spatially evolving wave field were performed in those studies for several fetches and two wind velocities in the test section of a midsize facility. Different stages in the development of the wave field were identified, and apparent contradictions between observations and the modulational instability theory were briefly discussed. Recently, experimental results on the evolution of waves along a tank under

steady wind forcing were compared in detail with numerical modeling [27]. The simulations clearly indicate that the nonlinearity of wind waves is the major factor that causes spectral variations in the course of spatial evolution and leads to a decrease of the spectral peak frequency f_p with the fetch x. Additional essential factor that had to be accounted for in the model in order to obtain quantitative agreement between the model predictions and measurements is the stochastic character of wind waves [4]. The modeling was therefore performed applying Monte Carlo simulations and using the spatial version of the Zakharov [28] equation and random initial conditions.

The understanding of relative importance of various physical mechanisms affecting the spatial evolution of young wind waves, i.e., wind input, nonlinearity, and dissipation, gained in the experimental and numerical study [27] are coupled here with the approach adopted in [26] to investigate the interaction of a quasimonochromatic deterministic wavemaker-generated wave with the waves excited by steady wind forcing. Experiments in a moderately sized wind-wave facility equipped with a computer-controlled wavemaker are performed for a range of constant wind velocities and a variety of wavemaker driving signals, including different wavemaker forcing frequencies f_{WM} and displacement amplitudes. For each set of operational conditions, interaction of the mechanically excited waves with wind waves is studied along the whole test section. Particular attention is given to the random character of wind waves and their interaction with the deterministic wavemaker-generated wave. The accumulated results allow us to draw conclusions regarding the effect of wind on the mechanically generated waves, as well as the influence of a deterministic wave on the evolution of wind waves along the test section and on their temporal and spatial coherence.

II. EXPERIMENTAL FACILITY AND PROCEDURE

The experiments were conducted in a wind-wave flume that consists of a closed-loop wind tunnel installed atop a 5-m-long, 0.4-m-wide, and 0.5-m-high test section (water depth is maintained at 19 cm). A computer-controlled blower enables the maximum wind speed in the test section up to about 15 m/s. Special care was taken to ensure uniform airflow in the test section. The tank is filled with distilled water to eliminate the formation of an elastic film on the surface that contributes to the damping of short waves. A flexible flap connects the bottom of the wind tunnel's converging nozzle to the test section slightly above the mean water level height to ensure smooth airflow. A wave energy absorbing beach made of porous material is placed at the far of the tank. The beach does not eliminate wave reflection completely, and measurements close to the far end of the test section may still be contaminated by the reflected waves. However, due to the fast decay of those waves that propagate against the wind, their contribution decreases rapidly with the distance from the far end. The effect of wave reflection therefore becomes negligible at fetches up to about 3.5 m (i.e., close to 1.5 m from the far end of the test section) [2–4].

This moderately sized experimental facility allows full control of the operational parameters, while enabling extensive and well-resolved accurate measurements that due to short time and space scales of the wave field do not require excessive duration of the experimental sessions. Detailed measurements of spatially evolving wind waves under steady wind forcing carried out for a wide range of wind velocities in our facility [4,8,27] demonstrated that the dimensionless power laws obtained in those studies do not differ significantly from the results of numerous field experiments in which the values of the wave age varied in a wide range; the updated summary of those experimental results are presented in [9,10]. Extensive measurements of the turbulent air flow in the test section above the waves provided the characterization of the logarithmic velocity profiles and of the interfacial shear stresses along the tank for different wind velocities [29].

A wedge-type wavemaker operated by a computer-controlled linear motor is used to generate a mechanical deterministic wave. The wedge is placed beneath the inlet flap upstream of the air inlet. The wavemaker motor is located above the test section and connected to the wedge by thin flat rods close to the sidewalls of the test section. This arrangement effectively prevents significant disturbance of the airflow by the wavemaker. The wavemaker is supported by an aluminum frame that is detached from the flume to eliminate any transfer of vibrations from the wavemaker to the

TABLE I. Representative wind velocities U and friction velocities u_* for different blower settings.

Blower setting no.	Maximum velocity U (m/s)	Friction velocity u_* (m/s)
1 (25%)	5.1	0.32
2 (30%)	6.3	0.41
3 (40%)	8.5	0.54
4 (50%)	10.6	0.68
5 (55%)	11.5	0.87

test section. The instantaneous water surface elevation along the centerline of the test section at any fixed distance x from the wind inlet (the fetch) is measured by four capacitance-type wave gauges made of the anodized tantalum wires and mounted on a bar parallel to the tank sidewall. The spacing between the adjacent probes is 10 cm. The bar with the gauges is supported by a vertical computer-controlled stage that has a positioning accuracy of 0.05 mm and is fixed to an instrument carriage that can be placed at any desirable location along the test section. The stage is used for static probe calibration. Wind velocity is monitored by a Pitot tube attached to the carriage and positioned at a height close to the center of the airflow part of the test section. The facility and the LabView-controlled experimental procedure, including operation of the blower, the wavemaker, the probe calibration, and the data acquisition, are visualized in [30]. Experiments on the spatial evolution of wind waves under steady wind forcing were carried out at five blower settings corresponding to wind velocities in the center of the test section ranging from $U = 5.1$ m/s to $U = 11.5$ m/s. The wind velocities for each blower setting and the corresponding representative friction velocities u_* are given in Table I.

The values of u_* are based on detailed measurements of the vertical velocity profiles as well as on independent measurements of the Reynolds stress distributions carried out in our facility [29]. At each wind velocity, data recordings were performed for five frequencies of the wavemaker driving signal f_{WM}, ranging from $f_{\mathrm{WM}} = 2$ Hz to $f_{\mathrm{WM}} = 6$ Hz.

It is well known [2,3,31] that for short gravity-capillary waves in the presence of wind, a non-negligible effect of the induced shear current on the dispersion relation of short gravity-capillary waves should be accounted for.

In the absence of wind, the wave number $k_{\mathrm{WM}} = 2\pi/\lambda_{\mathrm{WM}}$ of the mechanically generated waves can be calculated using the dispersion relation for free gravity-capillary waves in water of finite constant depth d:

$$\omega^2 = gk(1 + \sigma k^2/g)\tanh(kd), \tag{1}$$

where g is the acceleration due to gravity and σ is the surface tension coefficient divided by density. The actual length λ_{WM} of the wavemaker-generated wave for a given frequency in the presence of the Doppler effect due to the shear current is somewhat longer than that predicted by (1), in particular for higher forcing frequencies. Calculations based on the modified dispersion relation given in [3] yield the lengths of the mechanically generated waves that vary from $\lambda_{\mathrm{WM}} = 6$ cm to 42 cm for $f_{\mathrm{WM}} = 2$ Hz. These wavelengths imply that the effect of capillarity is relatively weak for waves at all wavemaker frequencies used in the present experiment and they are dominated by gravity; in fact, capillarity is only felt marginally at the two higher values of f_{WM} of 6 and 5 Hz; for lower values of f_{WM}, the mechanically generated waves can be seen as pure (albeit short) gravity waves.

At each wavemaker frequency, three wavemaker displacement amplitudes, 2.5, 5, and 10 mm, were applied. The values of wave amplitudes and steepness measured close to the inlet in the absence of wind for different wavemaker forcing conditions are presented in Table II for reference.

TABLE II. Parameters of wavemaker generated waves measured at $x = 0.17$ m.

Frequency (Hz)	Wm amplitude (mm)	Wave amplitude (mm)	Wave steepness (a^*k)
2	2.5	2.0	0.02
	5	3.6	0.05
	10	7.5	0.11
3	2.5	2.0	0.06
	5	3.2	0.10
	10	7.2	0.21
4	2.5	1.8	0.09
	5	3.0	0.15
	10	7.0	0.36
5	2.5	1.3	0.12
	5	2.4	0.22
	10	2.8	0.28
6	2.5	1.2	0.12
	5	2.2	0.23

Note that the wavelengths in Table II were calculated using (1). In the presence of wind, the wave numbers at those frequencies are reduced and become longer due to the Doppler shift in the presence of shear current, while the amplitudes are reduced by enhanced breaking. The actual steepness values of the mechanically generated waves are therefore notably lower than those of mechanically generated waves.

Measurements were also performed for pure wind waves (no wavemaker). Thus, experiments were carried out for nearly 100 different operational conditions. Measurements were performed at eight locations of the instrument carriage resulting in 32 wave gauge locations covering fetches from $x = 17$ cm to $x = 347$ cm. For each carriage position and operational conditions (the wind velocity U, the frequency f_{WM}, and the displacement amplitude of the wavemaker), continuous sampling of data provided by the four wave gauges at a frequency of 300 Hz/channel was carried out for at least 1 h to provide statistically reliable parameters. Therefore, the experimental session at a single carriage location along the test section for a given wind velocity, including the calibration of the probes after each measurement, lasts for several days. Such extensive measurements were feasible due to the application of the fully automatic LabView-controlled measurement procedure in a moderate-sized facility. In view of the variety of experimental conditions and multiple measurement locations, only selected representative results are presented in sequel.

III. RESULTS

A. Wave power spectra

Averaged frequency power spectra of the surface elevation $P(f_i)$ were calculated for all fetches for each set of the operational conditions. To this end, each continuous 1-h-long record was divided into 72 segments with a duration of 50 s each, and the power spectra with the frequency resolution of 0.02 Hz averaged over all segments were computed. For presentation of the measured discrete power spectra are presented here at the reduced resolution of 0.2 Hz. To identify principal qualitative features that characterize the evolution along the test section of wind-wave spectral shapes in the presence of a mechanically generated regular wave, we consider first the two extreme wavemaker frequencies and the two extreme wind velocities employed in the present experiments. The effect of wind on the evolving spectral shapes of a wave generated by the wavemaker operating at

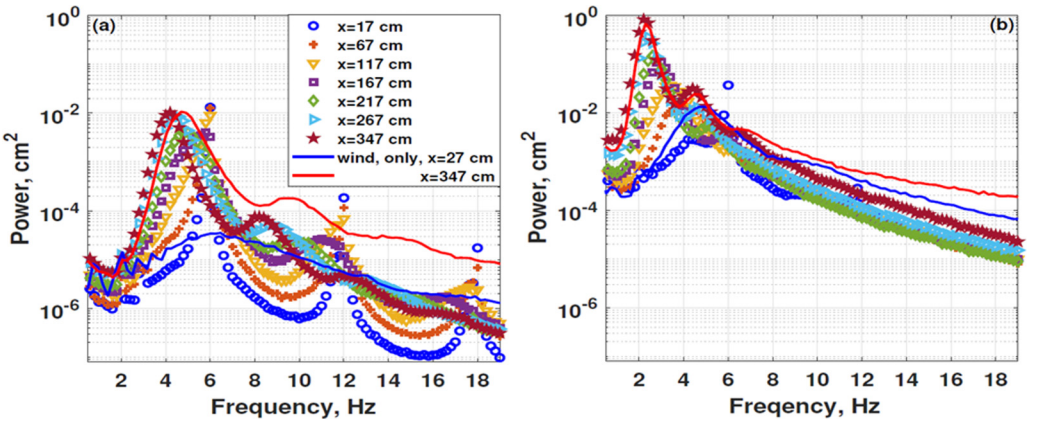

FIG. 1. Discrete wave power spectra for wavemaker frequency $f_{WM} = 6$ Hz and displacement amplitude 5 mm: (a) $U = 5.1$ m/s; (b) $U = 11.5$ m/s.

the intermediate vertical displacement amplitude of 5 mm is examined in Fig. 1 for the highest employed in the present experiments wavemaker frequency 6 Hz and in Fig. 2 for the lowest $f_{WM} = 2$ Hz. In both cases, the results are presented for a moderate wind velocity $U = 5.1$ m/s in panels (a) and for a much stronger wind with $U = 11.5$ m/s in panels (b). In all panels, the measured wave power spectra are plotted for several fetches; the spectra of pure wind waves measured close to the wind inlet and at a remote fetch are also plotted as a reference.

The results in Fig. 1(a) correspond to a case when the wavemaker frequency $f_{WM} = 6$ Hz is within the domain of naturally excited by wind at this velocity waves at short fetches, as seen from the spectrum of pure wind waves at $x = 27$ cm. Close to the inlet, the mechanically generated wave strongly affects the spectra that are dominated by a pronounced peak at the forcing frequency of 6 Hz, while the excitation by wind of waves at frequencies below about 5 Hz is suppressed as compared to the wind-wave case. The local peak with an initially high amplitude at 6 Hz is retained up to about $x = 0.7$ m, and then gradually decreases with fetch at the expense of widening and frequency downshifting of the spectrum. At fetches exceeding about 2 m, the peak at 6 Hz cannot be identified anymore, and the peak frequency $f_p(x)$ downshifts with fetch to increasingly lower values. At those fetches, the wave energy is mostly associated with frequencies well below the peak frequency of the pure wind waves, while at frequencies above $f_p(x)$, the wave energy in the presence of the wavemaker-generated wave is well below that measured for the pure wind waves at the corresponding frequencies. Note also that at shorter fetches, local sharp peaks at the second ($f = 12$ Hz) and third ($f = 18$ Hz) harmonics of the forcing frequency f_{WM} are clearly visible; their high peak amplitudes are apparently attained at the expense of the energy of waves at nearby frequencies. However, those peaks at higher harmonics decay very fast and cannot be identified at more remote fetches. This loss of energy of short steep waves can be attributed in part to their breaking that is enhanced by wind. Starting from about $x = 2$ m, a much wider peak corresponding to frequencies around the second harmonic and, to some extent, around higher harmonics of the local dominant frequency becomes clearly visible in the spectra. Those peaks are routinely observed in evolving nonlinear deterministic wave trains [32] as well as in random wind waves [4] and correspond to bound waves at the corresponding orders. The wave spectra obtained for the same wavemaker amplitude and frequency, but for much higher wind velocity ($U = 11.5$ m/s), are plotted in Fig. 1(b). The stronger wind causes much faster wave energy growth and peak frequency downshifting with fetch. In the presence of the mechanically generated wave at $f_{WM} = 6$ Hz, both the peak frequency and the wave amplitude at the far fetch are not very different from those observed for pure wind waves.

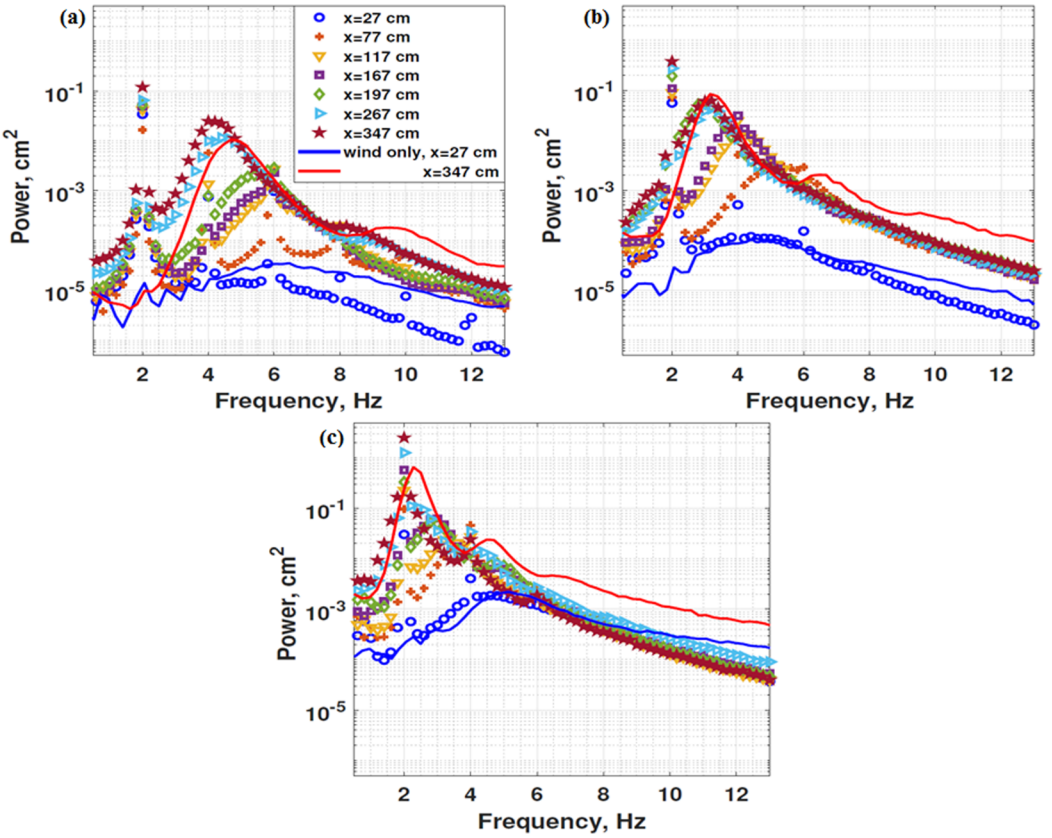

FIG. 2. Discrete wave power spectra for wavemaker frequency $f_{\mathrm{WM}} = 2\,\mathrm{Hz}$ and displacement amplitude 5 mm: (a) $U = 5.1\,\mathrm{m/s}$; (b) $U = 8.5\,\mathrm{m/s}$; (c) $U = 11.5\,\mathrm{m/s}$.

For this strong wind, the wavemaker excited wave dominates the spectrum only at very short fetches, $x < 0.5\,\mathrm{m}$; at longer fetches the peak frequency of waves shifts to values well below $f_{\mathrm{WM}} = 6\,\mathrm{Hz}$, and the initial effect of the regular waves gradually vanishes. Nevertheless, at more distant fetches the initial presence of the mechanically generated wave seems to result in a notable decrease of wind-wave energy at frequencies above the local peak frequency as compared to a pure wind wave. The local peaks at higher harmonics of the wavemaker frequency are much less pronounced in Fig. 1(b) than in Fig. 1(a); the peak at $f = 18\,\mathrm{Hz}$ practically vanishes at all fetches, while the second harmonic peak at $f = 12\,\mathrm{Hz}$ is only visible at the shortest fetch, $x = 17\,\mathrm{cm}$. Note also that in comparison with Fig. 1(a), stronger wind and consequently higher waves lead to the appearance of a wider peak associated with bound waves around the second harmonic of the peak frequency already starting from about $x = 1\,\mathrm{m}$.

Although the wavemaker frequency of $f_{\mathrm{WM}} = 2\,\mathrm{Hz}$ in Fig. 2(a) is well below the spectral domain of pure wind waves at short fetches and moderate wind forcing ($U = 5.1\,\mathrm{m/s}$), the measured wave energies at all fetches are significantly affected by the mechanically generated waves. Closer to the inlet, for fetches $x < 2\,\mathrm{m}$, the wave spectra in Fig. 2(a) may be divided into two frequency domains that at first glance seem to be well separated. The first domain at frequencies around the excited deterministic wave is characterized by a peak at $f = f_{\mathrm{WM}}$; the initial gradual widening of this peak is followed by the peak height growth with fetch. The second domain at frequencies exceeding about 3 Hz apparently contains random wind waves. These two spectral ranges, however, are in fact not fully decoupled. The initial spectrum at the shortest fetch of $x = 27\,\mathrm{cm}$ is characterized not

only by a prominent peak at the wavemaker driving frequency of 2 Hz, but also by the presence of multiple local peaks at higher harmonics of f_{WM}. In fact, at this fetch there is practically no wave energy contained beyond the close vicinity of f_{WM} and its higher harmonics; even the fifth and sixth harmonics at 10 and 12 Hz, respectively, can be clearly distinguished in the wave spectrum measured at $x = 17$ cm. The higher harmonics decay fast with fetch; nevertheless, the height of the third harmonic peak at 6 Hz grows up to about $x = 150$ cm, whereas the height of the second harmonic peak at 4 Hz continues to increase with fetch along the whole test section. A closer look at the spatial evolution of the initial peak at $f_{WM} = 2$ Hz reveals that for $x < 1$ m the peak widens with the increase in x, while the peak amplitude decreases somewhat with fetch, but farther away from the inlet it resumes its growth. Secondary peaks initially associated with higher harmonics also widen with fetch and eventually disappear, whereas the whole spectrum shifts to lower frequencies. Note also that the energy of the lower frequency part of the spectrum starting from about $x = 2$ m exceeds notably the energy of pure wind waves attained at the farthest fetch $x = 347$ cm that has a peak at frequency below 5 Hz. Also, at x beyond about 150 cm, a wider secondary peak centered at the second harmonic of the local peak frequency is clearly identifiable in the spectra. At higher wind, $U = 8.5$ m/s, Fig. 2(b), the spectral shape of the wind-wave part of the spectrum at $x = 3.37$ m is quite close to that of the pure wind wave spectrum at a comparable fetch, although the spectral peak frequency is slightly lower than that of pure wind waves. Remarkably, the spectral energy of the wind-wave components at frequencies exceeding about 5 Hz is suppressed and remains notably below that of pure wind waves at all fetches. The energy of the spectral peak corresponding to the regular wave component increases with fetch significantly and attains higher values as compared to a weaker-wind case in Fig. 2(a). At even higher wind velocity, $U = 11.5$ m/s, Fig. 2(c), the energies of the spectral components at frequencies exceeding the third harmonic of f_{WM} nearly do not vary with fetch and remain significantly below the corresponding values for pure wind waves. At frequencies below $3f_{WM}$, however, the wavemaker-related frequencies dominate the spectrum at short fetches, suppressing all other spectral harmonics as compared to their amplitudes in pure wind-wave field.

The growth with fetch of amplitudes at the peak frequency f_{WM} is accompanied by the spectral widening. The amplitudes of the second and third harmonics of f_{WM} are also well pronounced at the last fetch, $x = 347$ cm. Note that for pure wind waves, the peak frequency f_p in the spectrum exceeds 2 Hz for all fetches while the peak wave energy of those waves is notably below the maximum value attained in the presence of the mechanically generated wave.

The effect of the initial amplitude of the mechanically generated wave is explored in Fig. 3 for $U = 10.6$ m/s and applying the three wedge displacement amplitudes employed in the present experiments. As expected, the amplitude of the wavemaker displacement has a significant effect on wave spectra at very short fetches that in all panels of Fig. 3 differ notably from the wave spectrum of pure wind waves measured at identical wind forcing conditions. The dominant spectral peak at f_{WM} increases with the wavemaker amplitude and its height continues to grow with fetch for smaller wavemaker amplitudes of 2.5 and 5 mm. However, at fetches exceeding about $x = 1$ m, the peak at f_{WM} ceases to grow and its height becomes essentially independent of the wavemaker amplitude. The spectral shapes at frequencies exceeding f_{WM} and short fetches are affected by the stronger wavemaker amplitude. The larger the wavemaker amplitude, the more pronounced are the spectral peaks at the higher harmonics of f_{WM} that dominate the wave spectra especially at the two larger wavemaker amplitudes and attract wave energy from the frequency harmonics in the vicinity of those peaks. However, all peaks associated with the wavemaker motion eventually decay with fetch; the higher the frequency, the faster the corresponding peak effectively vanishes. At the largest fetch of $x = 347$ cm, the resulting wave spectra for all wavemaker amplitudes seem quite similar and do not differ significantly from the wave spectrum of pure wind waves. Since for $x > 1$ m, the steepness of the mechanical wave ceases to be affected by the wavemaker displacement amplitude, the suppression of higher frequencies in wind waves' spectra by the mechanical wave at $f_{WM} = 3$ Hz, while apparently existing, does not depend on the amplitude of mechanical forcing.

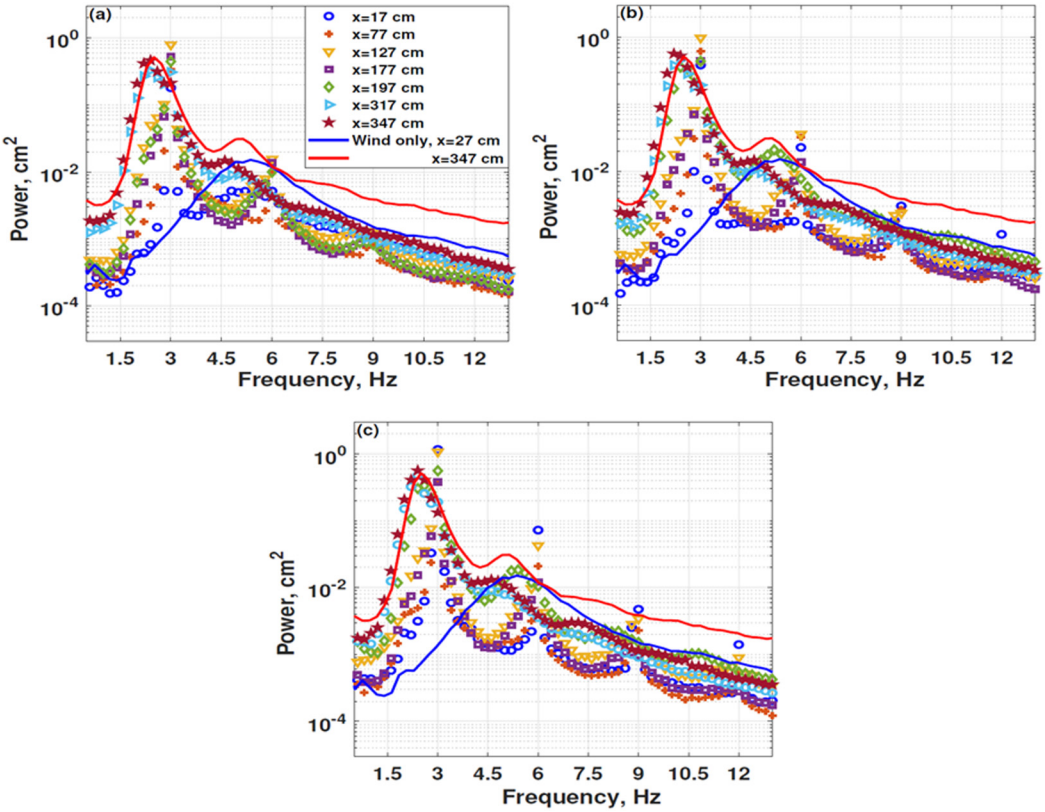

FIG. 3. Wave power spectra for wind velocity $U = 10.6$ m/s, wavemaker frequency $f_{\mathrm{WM}} = 3$ Hz, and three wavemaker displacement amplitudes: (a) 2.5 mm; (b) 5 mm; (c) 10 mm.

The prominence in the spectra of the higher harmonics of the wavemaker frequency at frequencies $f_n = nf_{\mathrm{WM}}$, in particular at short fetches and for weaker winds, prompted a closer look at those spectral components that can be naturally associated with higher-order bound waves. The bound waves are present when the wave nonlinearity is essential and cause deviation of the wave shape from sinusoidal [33,34]. The radian frequencies $\omega_n = 2\pi n f_{\mathrm{WM}}$ and the wave numbers $k_n = nk_{\mathrm{WM}}$ of bound waves are directly related to the corresponding values of free waves excited by the wavemaker.

The bound waves do not satisfy Eq. (1) and their phase velocities ω_p/k_p are identical to those of the mechanically generated free waves, $c_p = \omega_{\mathrm{WM}}/k_{\mathrm{WM}}$, thus being notably different from those of free waves at identical frequencies. This difference in phase velocities is utilized to establish the nature of wave components corresponding to the spectral peaks at the higher harmonics of the wavemaker frequency in the spectra presented in Figs. 1–3. Since the instantaneous surface elevation is measured simultaneously by four wave gauges equally spaced along the test section, the phase velocity of each harmonic can be determined from the cross-covariance coefficients of the surface elevation variation at the corresponding frequency $\eta(\omega_n, t)$ measured at different fetches, x_1 and x_2:

$$r_{1,2}(\omega_n, \tau) = \frac{\int_{T_0}^{T_0+\Delta T} \eta\left(\omega_{n,x_1}, t\right)\eta\left(\omega_{n,x_2}, t+\tau\right)dt}{\sqrt{\overline{\eta\left(\omega_{n,x_1}\right)^2}\,\overline{\eta\left(\omega_{n,x_2}\right)^2}}}, \tag{2}$$

where T_0 corresponds to the initial instant of the segment of the corresponding record, and the duration of integration ΔT is taken as several wave periods $2\pi/\omega_n$. The resulting value of $r_{1,2}(\omega_n,\tau)$

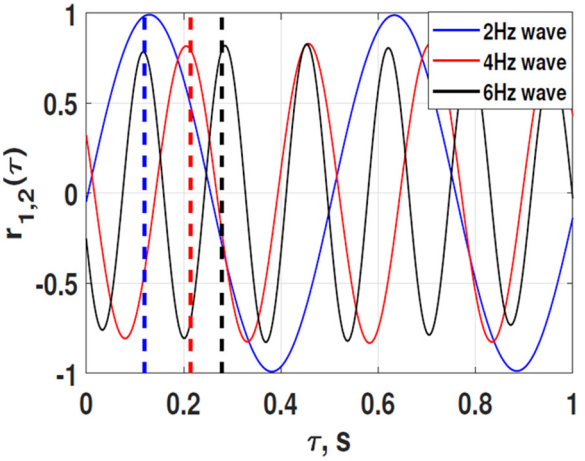

FIG. 4. The variation of the cross-covariance coefficient $r_{1,2}$ as a function of the time delay for measurements performed at $x_1 = 17\,\text{cm}$, $x_2 = 27\,\text{cm}$ for three frequencies corresponding to the local peaks in the spectra for the wavemaker frequency $f_{\text{WM}} = 2\,\text{Hz}$, the displacement amplitude 2.5 mm, and the wind velocity $U = 6.3\,\text{m/s}$. The vertical broken lines correspond to time delays for the phase velocities calculated using $c_p = \omega_{\text{WM}}/k_{\text{WM}}$.

is obtained by averaging the results for multiple segments, as in computation of the wave frequency spectra. The phase velocity of each harmonic thus is calculated as $c_p(\omega_n) = (x_2 - x_1)/\tau_{\max}$, where $\tau_{\max}$ corresponds to the maximum of $r_{1,2}(\omega_n,\tau)$. To obtain the values of $r_{1,2}(\omega_n,\tau)$ from the experimental data, the measured temporal records of the surface elevation were a narrow band-pass filter around ω_n, divided into 10-s-long segments, and the cross-covariance coefficients calculated for each segment using Eq. (2) were averaged over multiple segments. The typical variation of $r_{1,2}$ with the time delay τ is plotted in Fig. 4 for the wavemaker frequency $f_{\text{WM}} = 2\,\text{Hz}$ and for its second and third harmonics with most pronounced spectral peaks. The vertical lines in Fig. 4 correspond to time delays τ expected for the maximum in $r_{1,2}$ obtained under the assumption that each harmonic propagates with the free wave phase velocity calculated applying the empirical correction to Eq. (1) suggested in [3]. For $f = 2\,\text{Hz}$, this empirical dispersion relation yields $c_p = 0.845\,\text{m/s}$, corresponding to wavelength $\lambda = 0.42\,\text{m}$.

Calculations of the cross-covariance coefficient $r_{1,2}$ as shown in Fig. 4 were performed for numerous pairs of wave gauges at the closest to the inlet measuring station, i.e., for gauge fetches $0.17\,\text{m} \leqslant x \leqslant 0.47\,\text{m}$. The resulting phase velocities were averaged over various gauge pairs, wind velocities U and wavemaker amplitudes, yielding $c_p = 0.836\,\text{m/s}$, with the rms value of the scatter in various measurements of about 1%. This result thus confirms that the harmonics directly excited by the wavemaker at $f_{\text{WM}} = 2\,\text{Hz}$ indeed propagate with the phase velocity that is very close to that obtained from the empirical dispersion relation. Free waves at $f = 4\,\text{Hz}$ propagate with phase velocity $c_p = 0.471\,\text{m/s}$ ($\lambda = 0.12\,\text{m}$), while for $f = 6\,\text{Hz}$, $c_p = 0.36\,\text{m/s}$ ($\lambda = 0.06\,\text{m}$) [3]. The propagation velocities of those higher harmonics obtained from the measured temporal variations of $r_{1,2}$ averaged over numerous pairs yield $c_p = 0.461\,\text{m/s}$ for the spectral component at 4 Hz and $c_p = 0.355\,\text{m/s}$ for the 6-Hz component. For both quantities, the scatter of the data is about 2%. Similar measurements performed for the higher wavemaker frequency $f_{\text{WM}} = 3\,\text{Hz}$ results in $c_p = 0.601\,\text{m/s}$ vs $c_p = 0.613\,\text{m/s}$ ($\lambda = 0.20\,\text{m}$) according to the modified dispersion relation. The averaged values of $r_{1,2}$ for the second harmonic at $f = 6\,\text{Hz}$ in this case result in $c_p = 0.352\,\text{m/s}$ (relative error 2.2%), again very close to the value predicted for the free waves. It should be noted that the maximum values of $r_{1,2}$ decrease notably for harmonics at even higher frequencies with $n > 3$, so no attempt was made to evaluate their propagation velocities.

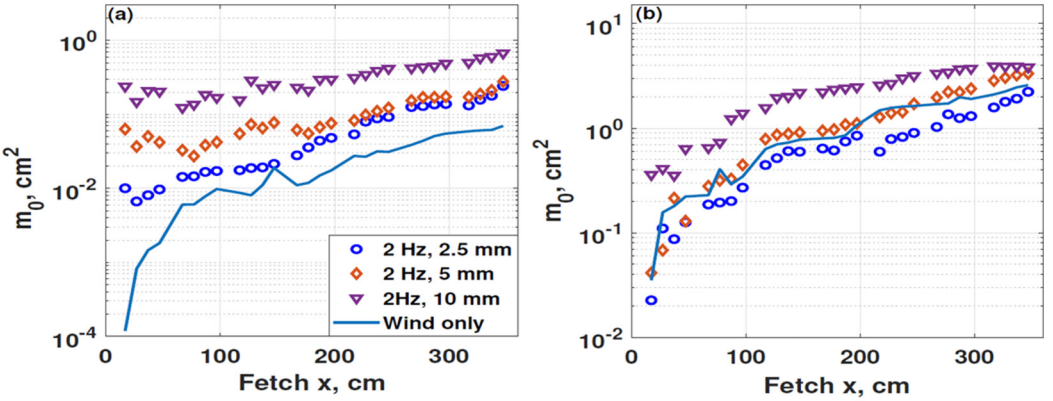

FIG. 5. Variation of the wave energy m_0 with fetch for the wavemaker operating at the driving frequency $f_{\mathrm{WM}} = 2\,\mathrm{Hz}$ and three displacement amplitudes for two wind velocities: (a) $U = 5.1\,\mathrm{m/s}$; (b) $U = 11.5\,\mathrm{m/s}$. The growth of the energy of pure wind waves is shown by a solid line.

These results demonstrate that free rather than bound waves constitute the dominant contribution to the spectral peaks at higher harmonics observed in Figs. 1 and 2. The appearance of free waves at frequencies $f = nf_{\mathrm{WM}}$ can be explained by the fact that due to wave nonlinearity, free waves at higher harmonics of the wavemaker frequency are necessarily generated by the wavemaker [32,35]. The nonpenetration condition at the wavemaker surface imposes equal amplitudes and opposite phases for the free and the bound wave harmonics at the flat surface of a wavemaker driven by a sinusoidal signal so that those high free and bound harmonics at the wavemaker location $x = 0$ cancel each other. For mechanically generated wave trains of limited duration, the different propagation velocities of free and bound waves eventually may lead to temporal separation of those waves at remote fetches (see, e.g., [36]). However, in the presence of wind, the free high-frequency harmonics initially grow fast with fetch and thus gain prominence; they only start to decay when the whole spectrum downshifts to significantly lower frequencies, mainly due to nonlinear interactions among various components [27].

B. Wave energy

The total wave energy is calculated as the sum of energies of all spectral components and thus corresponds to the zeroth spectral momentum m_0. The jth spectral moment for the discrete power spectrum $p(f_{\mathrm{j}})$ is defined as

$$m_j = \sum_{i_{\min}}^{i_{\max}} f_i^j p(fi), \tag{3}$$

where $i_{\min}$ and $i_{\max}$ define the domain of frequency harmonics over which the summation is carried out. The effect of the addition of a deterministic quasimonochromatic wave with different initial amplitudes on the variation of m_0 along the test sections is now examined. The variation of the total wave energy calculated over the interval $1\,\mathrm{Hz} \leqslant f_i \leqslant 12\,\mathrm{Hz}$ is presented in Fig. 5. The results for the wavemaker forcing frequency $f_{\mathrm{WM}} = 2\,\mathrm{Hz}$ for the weakest wind forcing in the test section corresponding to $U = 5.1\,\mathrm{m/s}$ are plotted in Fig. 5(a), while for the highest wind velocity, $U = 11.5\,\mathrm{m/s}$ in Fig. 5(b). In the absence of the mechanically generated wave, the total wave energy of pure wind waves m_0 initially rapidly increases from very low values at $x = 17\,\mathrm{cm}$ corresponding to the nearly negligible ripples; the initial fast growth with fetch then slows down and the dependence $m_0(x)$ approximated as $m_0 \sim x^n$ becomes close to linear, with $n \approx 1$ [8,23]; see also [7]. The addition of the mechanically generated wave results in the wave energy that at the initial fetch is larger by

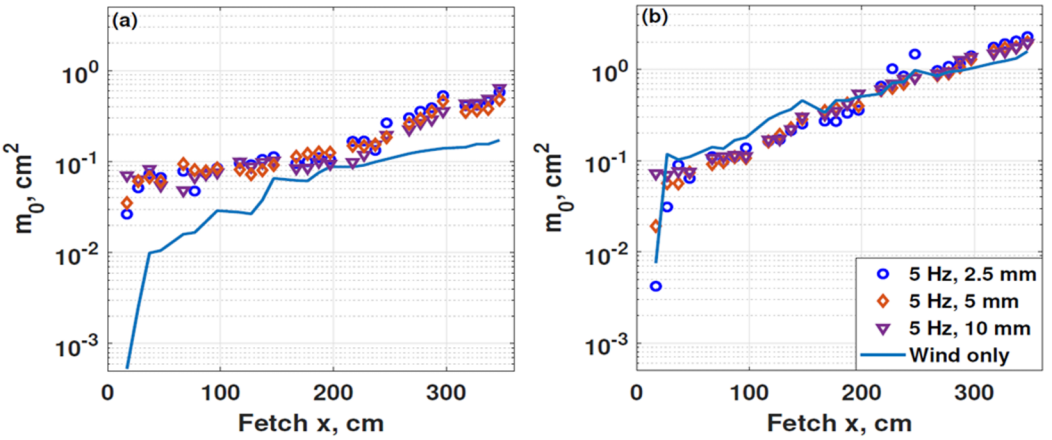

FIG. 6. As in Fig. 5, but for $f_{\mathrm{WM}} = 5\,\mathrm{Hz}$ and (a) $U = 6.3\,\mathrm{m/s}$; (b) $U = 10.6\,\mathrm{m/s}$.

orders of magnitude than that in the pure wind-wave field, with larger wavemaker displacement amplitude corresponding to higher initial wave energy.

This wave energy excess due to the wavemaker action is preserved in Fig. 5(a) along the whole test section, although the difference of the wave energies for different wavemaker amplitudes seems to decrease with fetch. For stronger wind forcing and thus more energetic wind waves, Fig. 5(b), the presence of the mechanically excited wave is less pronounced. Nevertheless, for the highest wavemaker displacement amplitude, the total wave energy exceeds that obtained in all other cases along the whole test section. For weaker and even for moderate wavemaker forcing, the total energy of the resulting wave field quite soon becomes comparable with that of pure wind waves. For larger fetches, there is a clear trend of closing the gap in the m_0 values, so that the effect of the initial conditions weakens with x. The effect of the wavemaker displacement amplitude is reduced significantly at higher wavemaker frequency, $f_{\mathrm{WM}} = 5\,\mathrm{Hz}$; see Fig. 6. In fact, the contribution of the wavemaker-generated wave is essential mainly for weaker wind and at short fetches, $x = 17\,\mathrm{cm}$ and $x = 27\,\mathrm{cm}$. Note also that for weaker wind forcing in Fig. 6(a), the wave energy in the presence of the mechanically generated waves exceeds that of the pure wind waves at all fetches; this however is not the case for stronger wind forcing where the values of m_0 are much less affected by the wavemaker action.

C. Characteristic frequencies and spectral width

The dominant frequency of a random wave field $f_{\mathrm{dom}} = m_1/m_0$ is customarily expressed using the spectral moments defined by Eq. (3), being a more robust characteristic than the peak frequency f_p. Usually, only free wave components are taken into account in the calculation of the moments. However, in a multimodal wave system as studied here, the distinction between the free and the bound components is not always straightforward and for that reason is not applied here. As observed in Fig. 2, for the wavemaker forcing frequency $f_{\mathrm{WM}} = 2\,\mathrm{Hz}$, the frequency domains associated with the mechanically generated and wind-excited waves can be separated, in particular for weaker wind forcing and for shorter fetches. In those cases, different dominant frequencies can be considered depending on the frequency domain selected in the calculation of the spectral moments m_{j}. The range $1\,\mathrm{Hz} \leqslant f \leqslant 2.5\,\mathrm{Hz}$ allows us to study the variation of the spectral distribution of wave energy in the vicinity of f_{WM}; the range $2.8\,\mathrm{Hz} \leqslant f \leqslant 12\,\mathrm{Hz}$ covers wind waves, however, they cannot always be distinguished from the higher harmonics of f_{WM} that are apparently related to the wavemaker action. Finally, the frequency range $1\,\mathrm{Hz} < f < 12\,\mathrm{Hz}$ covers all energy containing harmonics in the spectrum. The variation with fetch of the local dominant frequencies is plotted

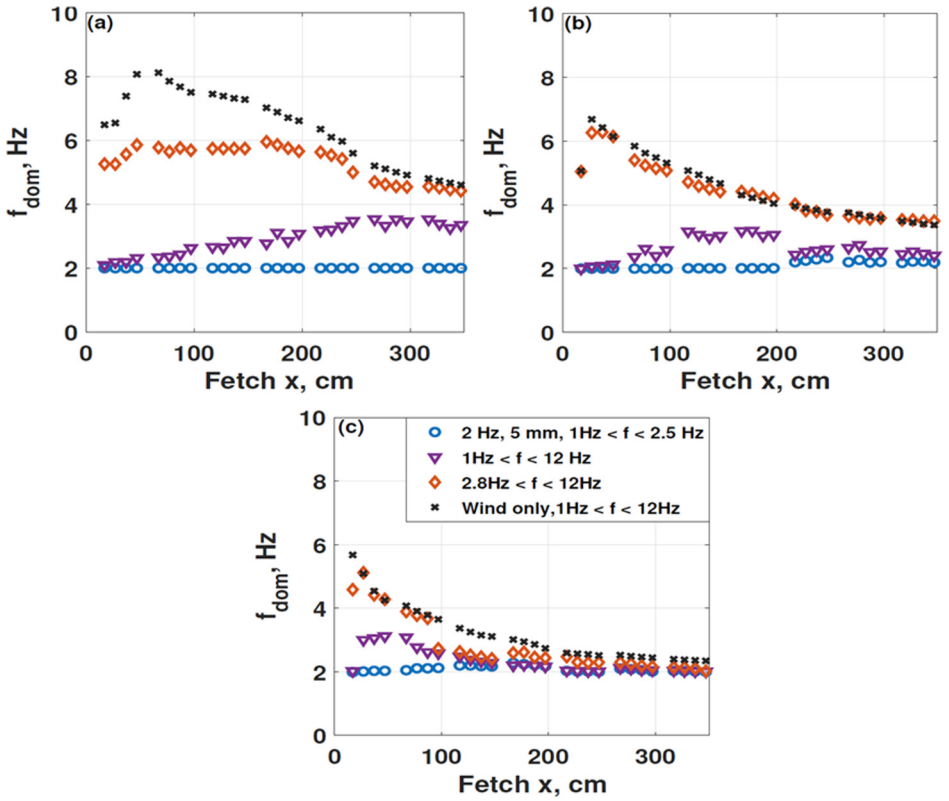

FIG. 7. The variation along the test section of dominant frequencies computed for various frequency domains; wavemaker frequency $f_{\mathrm{WM}} = 2\,\mathrm{Hz}$, displacement amplitude 5 mm: (a) $U = 5.1\,\mathrm{m/s}$; (b) $U = 8.5\,\mathrm{m/s}$; (c) $U = 11.5\,\mathrm{m/s}$.

in Fig. 7 for those three ranges of frequencies. In addition, the fetch dependence of the dominant frequency of pure wind waves calculated over the range $1\,\mathrm{Hz} \leqslant f \leqslant 12\,\mathrm{Hz}$ is also plotted. For relatively weak wind forcing, Fig. 7(a), the dominant frequency calculated over all frequencies in the spectrum exceeds slightly the wavemaker frequency $f_{\mathrm{WM}} = 2\,\mathrm{Hz}$ close to the inlet, where the wind waves are very small, and then increases with the fetch as the contribution of higher frequencies excited by wind enlarges. At fetches beyond about $x = 250\,\mathrm{cm}$, the values of f_{dom} cease to grow due to downshifting of the wind-generated part of the spectrum. The values of f_{dom} computed for the frequency domain around f_{WM} remain constant at 2 Hz; thus, the wavemaker-generated wave continues to dominate the spectrum in this frequency range at all fetches. The fetch dependence of the dominant frequency in the spectral domain that can be attributed to wind waves is qualitatively similar to that of pure wind waves, increasing initially with the fetch and then downshifting to lower values. However, the dominant frequencies characterizing this part of the spectrum are consistently below those obtained for pure wind waves over all frequencies. This can be attributed in part to the relative prominence of the second (4 Hz) and of the third (6 Hz) harmonics of f_{WM} in the spectrum; see Fig. 2.

For intermediate wind forcing, Fig. 7(b), wind waves become higher, and their contribution to f_{dom} increases. At short fetches, the energy of wind-generated waves is concentrated at higher frequencies, nevertheless the dominant frequency at the shortest fetch of $x = 17\,\mathrm{cm}$ is still determined by the wavemaker frequency f_{WM}, but then increases with the fetch. Due to downshifting with the fetch of the wind-wave part of the spectrum as seen in Fig. 7(b), the values of f_{dom} cease to

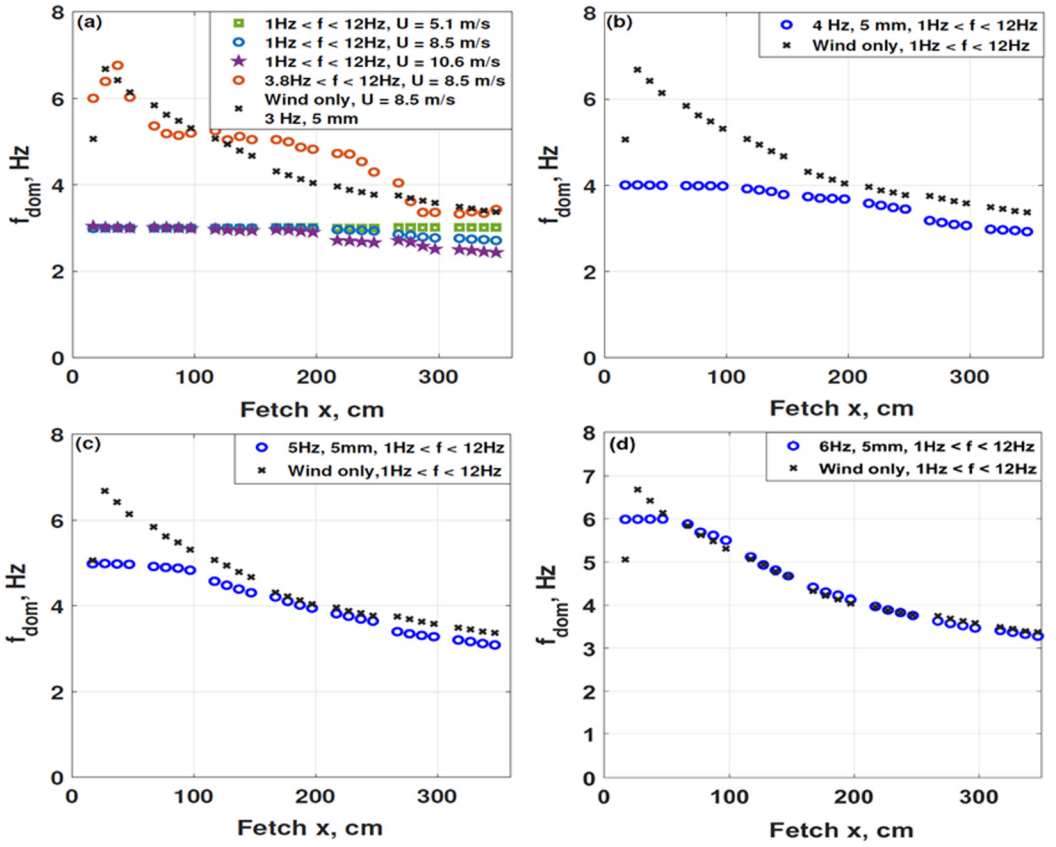

FIG. 8. The variation along the test section of the dominant frequencies computed for the wind velocity $U = 8.5\,\mathrm{m/s}$ and various wavemaker frequencies with the displacement amplitude of 5 mm.

grow from about $x = 100\,\mathrm{cm}$ and then decrease for $x > 200\,\mathrm{cm}$. At those more distant fetches, the reduction of frequencies of the energetic wind waves is accompanied by the widening of the spectrum around the wavemaker frequency and the growing contribution of spectral harmonics at frequencies exceeding f_{WM}. Note also that, starting from about $x = 200\,\mathrm{cm}$, the effect of the deterministic wavemaker-generated wave on the dominant frequency calculated for the wind-generated part of the spectrum only vanishes; it becomes nearly identical to f_{dom} of the pure wind wave calculated for the whole spectrum. A similar pattern is observed for even stronger wind forcing and correspondingly higher wind waves, Fig. 7(c), where the effect of the wavemaker-generated wave becomes very minor already at shorter fetches. The effect of the mechanically generated wave on the dominant frequency is examined in Fig. 8 for higher wavemaker frequencies, $3\,\mathrm{Hz} \leqslant f_{WM} \leqslant 6\,\mathrm{Hz}$. At those frequencies (with a possible exception of $f_{\mathrm{WM}} = 3\,\mathrm{Hz}$), there is no separation of frequency domains of the deterministic wavemaker generated and the random wind waves. Thus, the dominant frequencies are mainly determined using spectral moments computed overall significant frequencies and compared with the variation with fetch of the values of f_{dom} in the pure wind waves. In the somewhat special case of $f_{\mathrm{WM}} = 3\,\mathrm{Hz}$, an attempt is made to calculate separately the dominant frequency of the higher frequency part of the spectrum for this wavemaker frequency as shown in Fig. 8(a). The variation of this parameter with fetch in general follows that of f_{dom} in the pure wind waves, although the slope of the curve fluctuates notably, presumably due to the changes in the contribution of the higher harmonics of f_{WM}; cf. Fig. 3(b). For all wavemaker driving frequencies in Fig. 8, the mechanically generated wave dominates the spectrum at short fetches

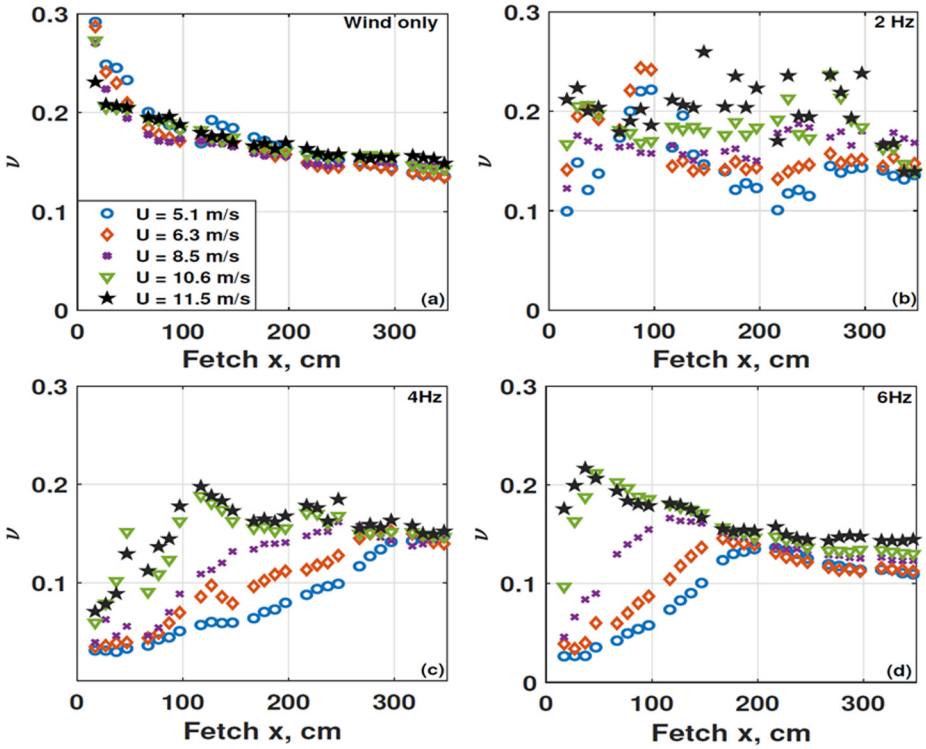

FIG. 9. The variation of the dimensionless spectral width ν along the test section for all wind velocities: (a) wind waves only; (b)–(d) wind and mechanically generated waves with wavemaker displacement amplitude of 5 mm at selected frequencies.

so that $f_{\mathrm{dom}} = f_{\mathrm{WM}}$; for more distant fetches the values of f_{dom} decrease with the fetch. This downshifting occurs earlier, and the effect of the mechanically generated waves decreases for higher values of f_{WM}. The contribution of the wavemaker-excited wave thus gradually becomes minor and effectively vanishes for $f_{\mathrm{WM}} = 6\,\mathrm{Hz}$; Fig. 8(d).

The dimensionless width of the spectrum ν defined using the spectral moments given by Eq. (1) as

$$\nu = \sqrt{\frac{m_0 m_2}{m_1^2} - 1} \tag{4}$$

represents an additional integral parameter characterizing the spectrum. The variation of ν with fetch is plotted in Fig. 9 for all wind velocities and several wavemaker frequencies; the fetch dependence of the dimensionless spectral width for the pure wind waves is also presented for comparison in Fig. 9(a). In the absence of the mechanically generated waves, the spectral width of the pure wind waves in the test section measured in the present experiments and plotted here as a reference decreases from around $\nu = 0.25$ to about $\nu = 0.15$; it does not exhibit meaningful dependence on the wind velocity, see Fig. 9(a), in agreement with experimental results [8,27]. Superposition of the wavemaker-generated waves significantly affects the variation of the spectral width with fetch at all wavemaker frequencies. For $f_{\mathrm{WM}} = 2\,\mathrm{Hz}$, Fig. 9(b), the spectrum at short fetches is dominated by the mechanically generated waves with only insignificant wave energy contained in the wind-wave part of the spectrum, see Fig. 2(a), resulting in an effectively narrow spectrum with small values of ν. Although the wave energy in the vicinity of f_{WM} increases with fetch, so also does the energy of the wind waves that is initially mainly associated with notably higher frequencies, leading to spectra with two distinct peaks and consequently to fast growth of the spectral width. The complex process

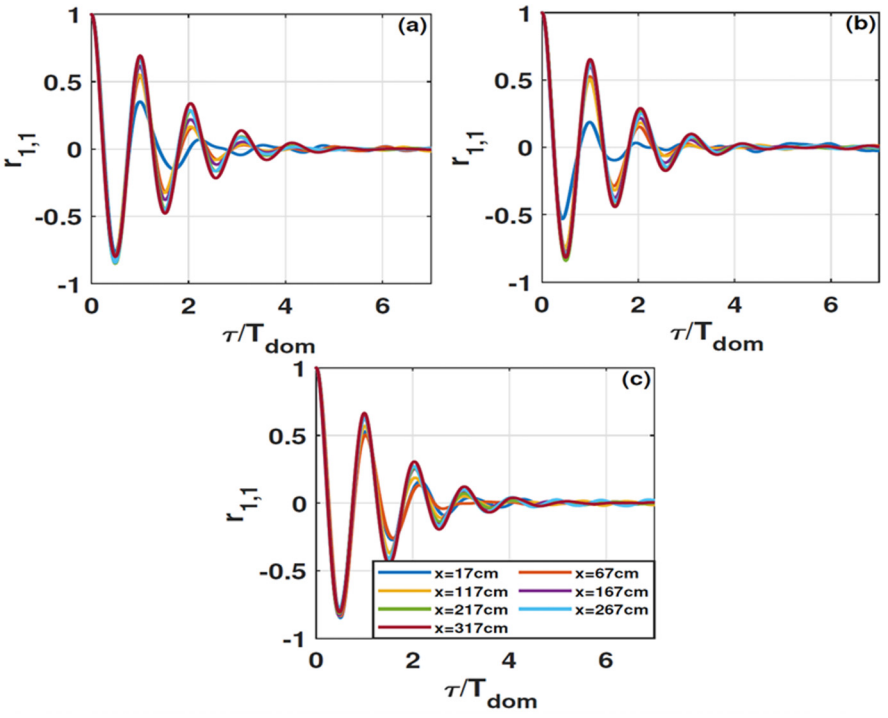

FIG. 10. The variation of the autocovariance coefficient $r_{1,1}(x,\tau)$ of the measured at several fetches, x surface elevation for the pure wind waves: (a) $U = 6.3$ m/s; (b) $U = 8.5$ m/s; (c) $U = 11.5$ m/s.

of downshifting of the wind-wave part of the spectrum combined with the nonlinear interactions of the wind waves with the mechanically generated wave results in a somewhat larger range of variation of ν with wind velocity for a given fetch and a larger scatter of data points in Fig. 9(b). Generally, for weaker winds, the domination of the mechanically generated waves is retained along the longer part of the test section leading to lower values of ν as compared to stronger winds where at fetches short enough, the wind waves become quite energetic at characteristic frequencies significantly larger than f_{WM}. The dimensional spectral width at those conditions thus may attain values close to $\nu = 0.25$. At longer fetches, the spectral domains of the wind and the mechanically generated waves gradually converge, see Fig. 2(b), leading to a decrease in the dimensionless spectral width to $\nu \approx 0.15$ for all wind velocities.

The variation of the dimensionless spectral width at higher wavemaker frequencies f_{WM} presented in Figs. 9(c) and 9(d) shows considerably less scatter than in Fig. 9(b), however, the overall behavior is similar. The spectral width increases first from very small initial values of ν at short fetches where the wavemaker frequency is within the spectral range of the pure wind waves, and then increases as the waves grow and the spectrum becomes broader, attaining the values of ν close to those in Fig. 9(a).

D. Temporal and spatial coherence

The present study deals with the interaction of the random wind-excited waves with a deterministic wave mechanically generated by the wavemaker. The interrelation between the regular and the random parts of the resulting wavefield can be analyzed using the auto- and cross-covariance functions. To provide the reference values, pure wind waves are considered first. The variation of the autocovariance coefficient $r_{1,1}(\tau)$ for those waves calculated using Eq. (2) for a selection of probe locations $x = x_1 = x_2$ is presented in Fig. 10 for three wind velocities. To facilitate comparison of

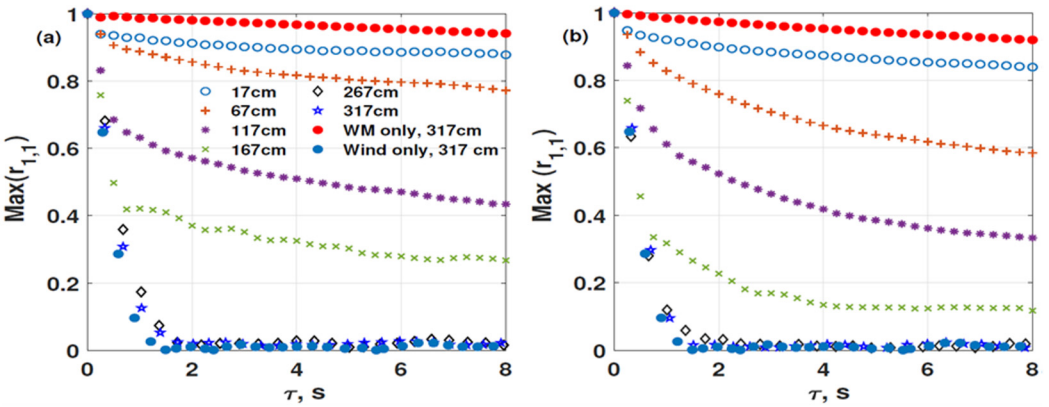

FIG. 11. The variation with fetch of the local maximum values of the autocovariance coefficient $r_{1,1}(x,\tau)$ of the surface elevation for the wind velocity $U = 8.5\,\mathrm{m/s}$, wavemaker frequency $f_{\mathrm{WM}} = 4\,\mathrm{Hz}$ with the displacement amplitudes: (a) 2.5 mm; (b) 10 mm.

the values of $r_{1,1}(\tau)$ at different fetches, the time delay τ is normalized in this figure by the local dominant wave period $T_{\mathrm{dom}}(x) = 1/f_{\mathrm{dom}}(x)$. The plots of $r_{1,1}(\tau/T_{\mathrm{dom}})$ for different wind velocities are surprisingly similar. At each fetch in all panels of Fig. 10, the values of $r_{1,1}$ oscillate with the local dominant frequency. The amplitudes of the oscillations decay fast so that at all fetches and at all wind velocities, the records of the surface elevation of pure wind waves show limited temporal coherence and become essentially uncorrelated after less than three dominant wave periods.

Except for the shortest fetch of $x = 17\,\mathrm{cm}$, there is only a moderate change in the absolute values of the three first local maxima at each fetch; at more remote fetches the values of $r_{1,1}(\tau/T_{\mathrm{dom}})$ become only weakly dependent on fetch. The loss of temporal coherence can be characterized by plotting the local maximum values of $r_{1,1}(\tau)$ that characterize amplitudes of $r_{1,1}$ oscillations.

The effect on the temporal coherence of the addition of the deterministic wavemaker-generated wave to the wave field evolving due to the wind action is demonstrated in Fig. 11 for wind velocity $U = 8.5\,\mathrm{m/s}$, the wavemaker frequency $f_{\mathrm{WM}} = 4\,\mathrm{Hz}$ and two wavemaker displacement amplitudes. The variation with fetch of the maximum values of $r_{1,1}(\tau)$ for pure wind waves and for mechanically generated waves in the absence of wind is also plotted for comparison. Note that no normalization of the time delay τ by the dominant wave period is applied here due to the existence of multiple-dominant frequencies for multimodal wave systems as shown in Figs. 7 and 8.

In the absence of wind, the deterministic wave retains its coherence for a long time for both wavemaker amplitudes, and the maxima of the autocovariance coefficient at a remote fetch remain well above 0.9 for the whole extent of τ that in Fig. 11 corresponds to 32 wavemaker forcing periods. Nevertheless, it can be noticed that for the larger wavemaker amplitude and thus large steepness of the initial deterministic wave, there is a certain increase in the rate of loss of wave coherence, presumably due to the enhancement of nonlinear effects that cause spectral broadening. Wind causes a notable decrease in the wave coherence already at a very short fetch of $x = 17\,\mathrm{cm}$. In both panels of Fig. 11, the maximum values of $r_{1,1}(x,\tau)$ decrease monotonically with fetch, and at fetches exceeding about $x = 2\,\mathrm{m}$, the rate of loss of coherence with fetch becomes practically identical to that of the pure wind waves. As long as the contribution of the deterministic wave remains notable, the spacing between the subsequent maxima in Fig. 11 is maintained at $\Delta\tau = 0.25\,\mathrm{s}$, so that the decaying oscillations of $r_{1,1}(\tau)$ occur at the wavemaker frequency f_{WM}. At longer fetches, the regularity of waves practically vanishes, and temporal spacing $\Delta\tau$ between the adjacent maxima is not constant anymore and becomes longer. Comparison with Fig. 8(b) demonstrates that this occurs when the values of the local dominant frequency decrease below f_{WM}. Note that the effect of the initial amplitude of the deterministic wave on the wave field coherence is relatively minor and

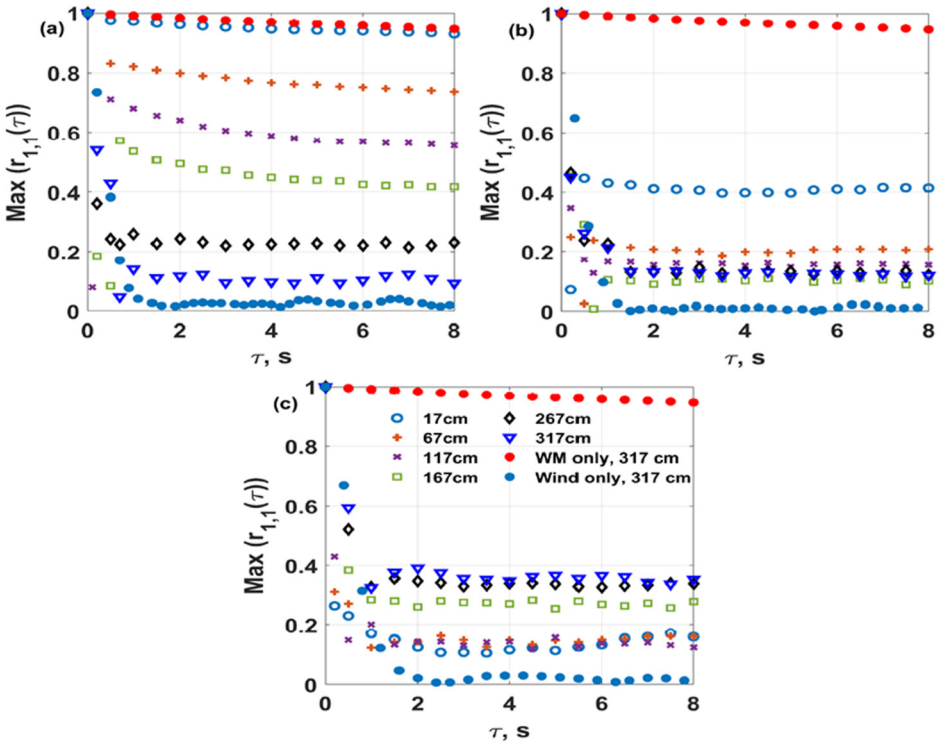

FIG. 12. As in Fig. 11 for the wavemaker frequency $f_{WM} = 2$ Hz with the displacement amplitude 2.5 mm for the wind velocities: (a) $U = 6.3$ m/s; (b) $U = 8.5$ m/s; (c) $U = 11.5$ m/s.

for all fetches, the shapes of $\max[r_{1,1}(\tau)]$ in Figs. 11(a) and 11(b) are quite similar. Nevertheless, the right panel of this figure exhibits a somewhat higher rate of coherence loss. Results at higher wavemaker frequencies, $f_{WM} = 5$ Hz and $f_{WM} = 6$ Hz are similar and thus not presented here. It should be noted, though, that randomization of the wave field with fetch in those cases occurs even faster.

The variation of $r_{1,1}(\tau)$ with fetch for lower wavemaker frequencies, $f_{WM} = 3$ Hz and $f_{WM} = 2$ Hz, appears to be quite different. The maxima of $r_{1,1}(x,\tau)$ are plotted in Fig. 12 for $f_{WM} = 2$ Hz, the wavemaker displacement amplitude of 2.5 mm, and three wind velocities. At this forcing frequency, the temporal coherence is not completely lost at all wind velocities. For a relatively weak wind ($U = 5.1$ m/s) in Fig. 12(a), the decay in coherence with fetch is monotonic as at higher wavemaker frequencies. There is, however, a qualitative difference between the behavior of $r_{1,1}(x,\tau)$ in this panel with that in Fig. 11 at longer fetches that were characterized by the total loss of coherence. Contrary to Fig. 11, the maximum values of $r_{1,1}(\tau)$ at $x = 317$ cm in Fig. 12(a) remain small but finite at larger time delays τ. For a relatively stronger wind with $U = 8.5$ m/s, Fig. 12(b), the loss of coherence with fetch is faster, and the lowest maximum values of $r_{1,1}(x,\tau)$ of about 0.1, not significantly different from the lowest values in Fig. 12(a), are attained already at about $x = 150$ cm. At longer fetches, there is no decrease in the maximum values of $r_{1,1}(\tau)$ and the level of coherence at this wind velocity even increases somewhat, attaining at more remote fetches $\max[r_{1,1}(\tau)] \approx 0.13$. An increase in the wind velocity to $U = 11.5$ m/s, Fig. 12(c), results in a very fast decrease in $r_{1,1}(x,\tau)$, so that already at the closest fetch, $x = 17$ cm, the maximum values attained by $r_{1,1}(\tau)$ become as low as about 0.1; however, for fetches exceeding about 1.5 m they resume their growth, reaching $\max[r_{1,1}(\tau)] \approx 0.35$ at the most remote fetches. In all panels of Fig. 12, the coherence is not fully lost everywhere along the test section and the spacing between

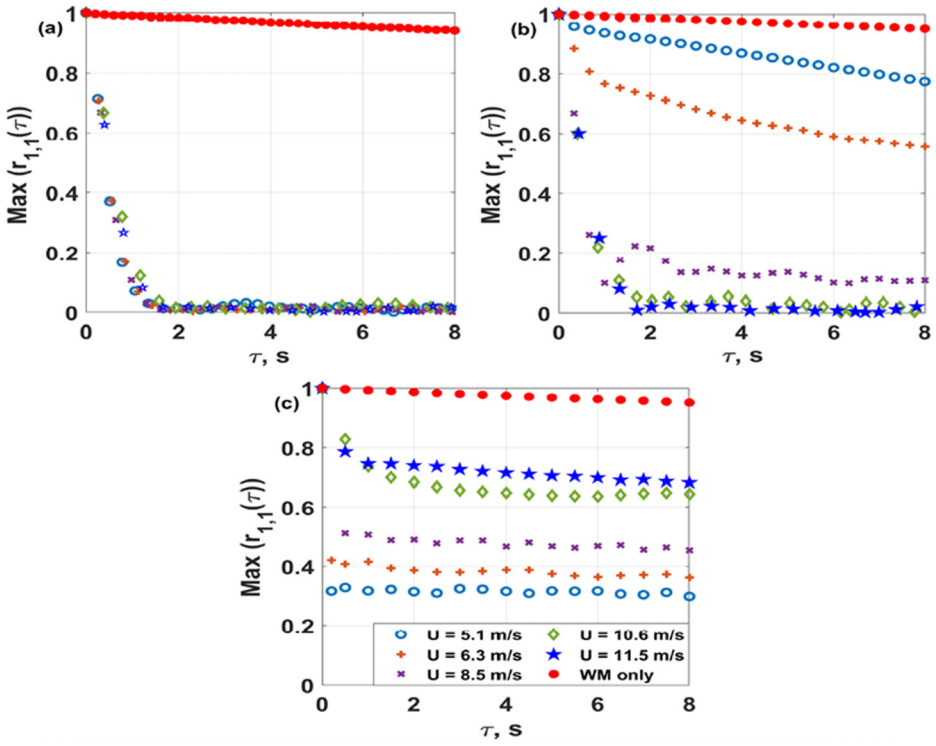

FIG. 13. The local maximum values of the autocovariance coefficient $r_{1,1}(x,\tau)$ of the surface elevation records at $x = 317$ cm, wavemaker displacement amplitude 5 mm, and various wind velocities for (a) $f_{WM} = 5$ Hz; (b) $f_{WM} = 3$ Hz; (c) $f_{WM} = 2$ Hz.

the adjacent maxima of $r_{1,1}(\tau)$ remains constant at $\Delta\tau = 0.5$ s, identical to the wavemaker driving signal period, $1/f_{WM}$.

The results on temporal coherence of wave systems consisting of an initially deterministic wave and random wind waves are summarized in Fig. 13, where the variation of $\max[r_{1,1}(\tau)]$ is presented at a single remote fetch ($x = 317$ cm) for all wind velocities applied in the present experiments and for several wavemaker forcing frequencies f_{WM}. For the higher wavemaker forcing frequency in Fig. 13(a), $f_{WM} = 5$ Hz, there is no persisting effect of the deterministic wave component on the wavefield coherence at this fetch. Fast loss of the temporal coherence occurs at all wind velocities, similarly to the stochastic behavior observed for the pure wind waves in Fig. 10; the records of the surface elevations become practically uncorrelated after a few dominant wave periods that at this location vary from about 0.2 s for the lowest wind velocity to 0.4 s for the strongest wind. At a lower wavemaker frequency, $f_{WM} = 3$ Hz, Fig. 13(b), the contribution of the deterministic wave components vanishes only at wind velocity exceeding $U = 8.5$ m/s, while for weaker winds the coherence is still not fully lost at this fetch. The complete and fast loss of coherence at higher wind velocities is practically identical to that observed for the pure wind waves. A substantially different pattern of variation the temporal coherence is observed at the lower wavemaker frequency, $f_{WM} = 2$ Hz, Fig. 13(c). Contrary to the behavior observed in Figs. 13(a) and 13(b), in Fig. 13(c) the maximum values of $r_{1,1}(\tau)$ at each wind velocity U do not change notably with τ. The regulating effect of the mechanically generated wave is retained over the whole length of the test section and for all wind velocities. However, the maximum values of $r_{1,1}(\tau)$ in panel (c) are low for the weakest wind in the present experiments, $U = 5.1$ m/s. The coherence of the wavefield increases with wind velocity, so that for the strongest wind forcing in the present experiments with $U = 11.5$ m/s, the

maximum values of $r_{1,1}(\tau)$ remain quite large for time delays τ exceeding 15 wavemaker periods, retaining the coherence level comparable to that measured for the mechanically generated waves in the absence of wind.

The salient feature of all plots in Figs. 10–13 is that as long as some degree of the temporal coherence is retained [the threshold value may correspond to maxima of $r_{1,1}(\tau)$ exceeding about 0.1], the spacing between the adjacent maxima of the autocorrelation function remains equal to the wavemaker period. This observation implies that the contribution of the initially deterministic wavemaker-generated wave remains essential in defining the temporal coherence of the evolving wind-wave field. To examine this property closer, it is instructive to analyze the coherence of the mechanically generated components as compared to other spectral harmonics for different operational conditions. The coherence between two signals in the Fourier frequency space is customarily assessed using the magnitude-squared coherence (MSC),

$$\mathrm{MSC}(f) = \frac{\left|P_{x_1,x_2}(f)\right|^2}{P(x_1, f)P(x_2, f)}, \tag{5}$$

where $|Px_1,\ x_2(f)|$ is the absolute value of the complex cross spectrum of the surface elevation signals $\eta(t)$ measured at fetches x_1 and x_2. The spatial coherence of surface elevation records $\eta(t)$ as a function of frequency defined by MSC is applied here rather than the autocovariance coefficient used so far to study the temporal coherence in the physical space for the spacing between the two wave gauges of 30 cm. Normalization by the corresponding power spectra values results in MSC being close to unity at frequencies where the correlation between the signals is significant and small otherwise. The spatial coherence of the measured wave field at various wavemaker forcing frequencies is presented in Fig. 14. The relatively large fetches of 317 and 347 cm chosen for calculation of MSC(f) allow us in particular to examine to what extent the initially regular wavemaker-excited wave retains its coherence in the presence of wind away from the wavemaker.

At the highest wavemaker frequency in Fig. 14, $f_{\mathrm{WM}} = 4\,\mathrm{Hz}$, some coherence of the mechanically generated harmonic is preserved at those fetches only for the lower wind velocity, $U = 5.1\,\mathrm{m/s}$, with MSC ≈ 0.3; for stronger winds, the values of MSC at this frequency become quite low. Note that no peak at the wavemaker forcing frequency was observed for MSC(f) computed for the higher values of the wavemaker forcing frequency, $f_{\mathrm{WM}} = 5\,\mathrm{Hz}$ and $f_{\mathrm{WM}} = 6\,\mathrm{Hz}$; those plots are therefore not presented. For $f_{\mathrm{WM}} = 3\,\mathrm{Hz}$, the MSC($f_{\mathrm{WM}}$) > 0.9 for $U = 5.1\,\mathrm{m/s}$; it remains notable also at larger wind velocities, attaining the value of 0.3 even at a high wind velocity of $U = 10.6\,\mathrm{m/s}$. At lower wind velocities of $U = 5.1\,\mathrm{m/s}$ and $U = 6.3\,\mathrm{m/s}$, MSC(f) features distinct peaks at the second harmonic of f_{WM}, $f = 6\,\mathrm{Hz}$, and even at the third harmonic, $f = 9\,\mathrm{Hz}$; see Fig. 14(b). When the wavemaker frequency is further decreased to $f_{\mathrm{WM}} = 2\,\mathrm{Hz}$, Fig. 14(c), the values of MSC(f_{WM}) exceed 0.95 at all wind velocities. At higher wind velocities, significant peaks in MSC are observed at higher harmonics of f_{WM}, up to the fourth wavemaker frequency harmonics at $f = 8\,\mathrm{Hz}$.

IV. DISCUSSION

The wavemaker forcing frequencies were selected in view of the measured spectra of pure wind waves in the facility. The initial detectable ripples usually have frequencies of about 7–8 Hz, corresponding to lengths of a few centimeters, while the longest waves at the far end of the test section under strong wind forcing may be longer than 40 cm at frequencies below 2 Hz [37,38]. To gain a better understanding of the wind effect on a deterministic wave and its interaction with wind waves, it would be desirable to apply the wavemaker forcing at frequencies that extend well beyond this range. Mechanical wave excitations at frequencies significantly lower than those characteristic for wind waves would allow modeling of interaction between wind-generated waves and swell. However, attaining full length- and time-scale separation in any laboratory facility can hardly be attained, certainly in a moderately sized test section in which the present experiments

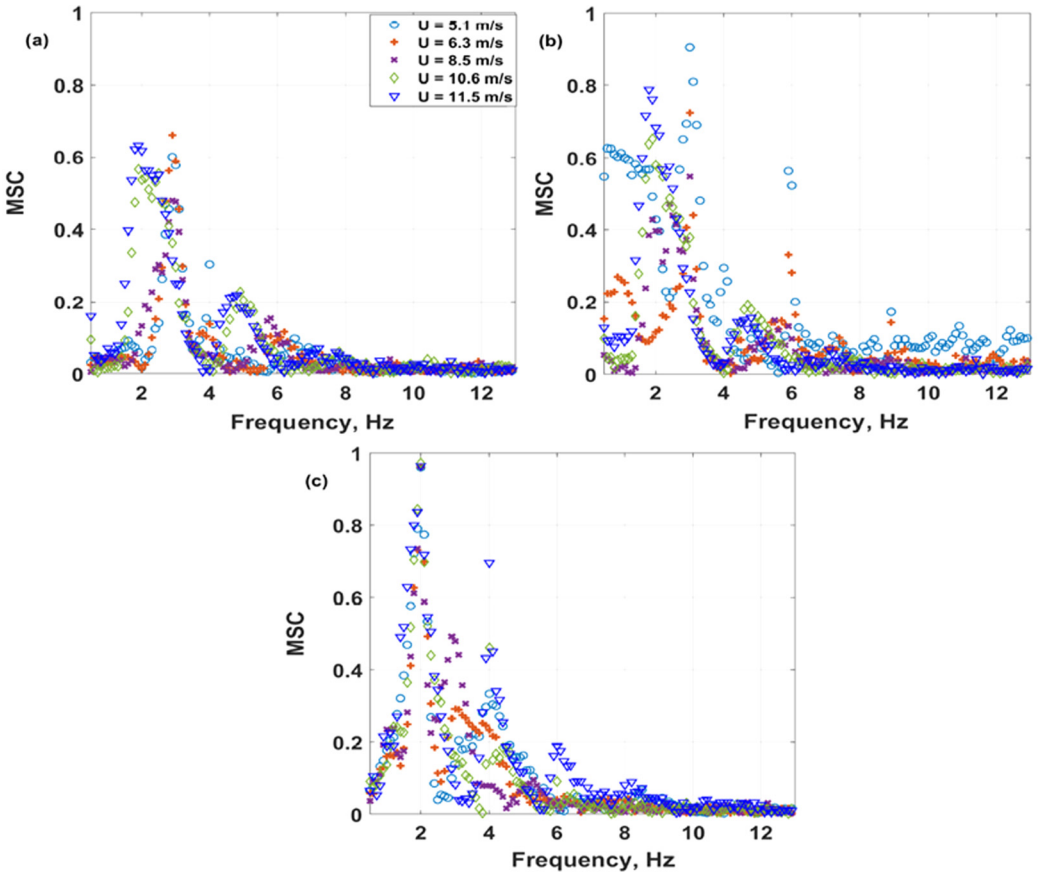

FIG. 14. The magnitude-squared coherence (MSC) of the surface elevation records at fetches $x_1 = 317$ cm and $x_2 = 347$ cm, wavemaker displacement amplitude 5 mm, and various wind velocities for (a) $f_{\mathrm{WM}} = 4$ Hz; (b) $f_{\mathrm{WM}} = 3$ Hz; (c) $f_{\mathrm{WM}} = 2$ Hz.

were performed. Still, even the incomplete scale separation between the regular mechanical and the random wind waves allows us to gain understanding on the nature of interaction among those waves.

The mechanical limitations prevented us from carrying out experiments at frequencies exceeding 6 Hz. This high-frequency restriction in fact proved to be nonexistent due to the observed excitation of regular free waves at the wavemaker at higher harmonics of the wavemaker frequency f_{WM} as discussed in Sec. III A. The results demonstrate that those regular waves at high frequencies initially dominate the spectrum, resulting in spectral shapes that are very different from those of pure wind waves. The notable initial growth of the high-frequency spectral components excited by the wavemaker is consistent with the assumption that wind input mainly occurs in the spectral vicinity of the local dominant frequency [27]. The prominence of high harmonics of f_{WM} in the wave spectra is however short-lived. The enhanced dissipation at high frequencies as well as nonlinear interactions of those steep waves with the adjacent spectral harmonics results in frequency downshifting of the whole spectrum. The contribution of the deterministic waves at frequencies well above the local peak frequency of the naturally evolving wind waves vanishes at more remote fetches. Thus, for higher wavemaker forcing frequencies, the spectral shapes, the dominant frequency and the spectral width, as well as the wave energy measured at more remote locations become practically indistinguishable from the corresponding parameters of pure wind waves, as seen in Secs. III A–III C. The amplitude of the wavemaker displacement at higher values

of f_{WM} has a limited effect on the wavefield at short fetches only. At longer fetches, the statistical parameters in the presence of the high-frequency wavemaker forcing become practically identical to those of the random wave field under steady wind forcing as studied in detail in our facility [8,39]. The effect of waves mechanically generated at frequencies below the local peak frequency of wind waves may be more substantial. As seen in Figs. 3 and 8(a), the wavemaker-generated wave at $f_{WM} = 3$ Hz causes faster spectral downshifting, apparently as a result of its dominance in the nonlinear interactions with the neighboring spectral harmonics and possibly also due to the enhanced wind input in the vicinity of f_{WM} in the presence of the dominant deterministic wave. As a result, the peak frequency at a remote fetch may be lower than that for waves excited by wind only.

The most pronounced manifestation of the effect of the mechanically generated wave on wind waves observed in Figs. 1–3 is the suppression of waves at frequencies exceeding that of the mechanical wave, as noticed by Mitsuyasu [11] and Donelan [13]. However, the results of Fig. 3 demonstrate that the suppression of the high-frequency part of the spectrum is not necessarily enhanced with an increase in the steepness of the mechanical wave, as suggested in [11]. The Phillips and Banner [12] mechanism that attempted to explain this phenomenon was shown to be too weak at stronger winds [40]. Donelan [13] and Masson [18] argued that the suppression of wind waves at higher frequencies is caused by nonlinear interactions. Nonlinearity indeed plays a significant role in the spectral evolution of the wind-wave field with the fetch, as demonstrated in [27]. The results of the present study, however, seem to support the sheltering mechanism explored in the theoretical model of Chen and Belcher [14] and verified experimentally by Bailey *et al.* [15]. The boundary layer separation from the crest of a longer wave observed in these experimental studies strongly affects the stress distribution and suppresses the generation of shorter waves.

Regarding the evolution of the lower part of the spectrum, of particular interest is the case with the wavemaker operating at the lowest frequency $f_{WM} = 2$ Hz. At this frequency, the wavemaker-excited wave can be seen as effectively decoupled from the growing with the fetch random wind waves, in particular for the lower wind velocities U. As seen in Figs. 7(b) and 7(c), the variation with the fetch of the dominant frequency of the wind part of the spectrum is practically not affected by the mechanically generated wave. The stronger effect of the wavemaker for the weaker wind in Fig. 7(a) results from higher relative contribution of the mechanically generated higher harmonics of f_{WM}. For stronger wind and at larger fetches, the separation between the frequency domains of the random and the deterministic waves gradually disappears, but contrary to lower wavemaker frequencies, the spectral peak at f_{WM} is retained in all panels of Fig. 2. The contribution of the components in the vicinity of $f_{WM} = 2$ Hz to the wave spectra remains significant at all fetches and wind velocities. Unlike in cases with higher f_{WM}, the variation of the wave energy with fetch remains dependent on the wavemaker displacement amplitude, see Fig. 5, though the relative contribution of harmonics associated with the initially regular wave decreases with the fetch and shows a tendency to vanish eventually.

While it is generally accepted that ocean waves in general, and wind waves in particular, are random and their stochastic behavior has to be accounted for in any attempt to model those waves, this aspect so far has not attracted adequate attention. Of course, the approach adopted in the derivation of the kinetic equation which serves as a basis of modern ocean wave models is based on the stochastic nature of waves [41]. Similarly, in the wave generation theory offered decades ago by Phillips [42], the randomness and the three dimensionality of wind waves play an important role. However, the stochastic wave aspects are often analyzed in terms the statistical moments of wave parameters and of deviation of the higher statistical moments from the values corresponding to the Gaussian distribution [43] where the role of wave coherence in the dynamics of extremely steep (rogue) waves in the ocean was analyzed. In a different approach the evolution of nonlinear random wind waves is modeled applying Monte Carlo simulation based on the spatial version of the Zakharov equation and multiple realizations with random initial conditions [27]. They demonstrated that in order to obtain quantitative agreement between simulations and measurements, it is essential to account for the loss of the wave coherence with fetch.

The limited temporal and spatial coherence of gravity capillary and short wind waves studied here is also of direct relevance to the investigations of the ocean surface based on radar remote sensing. The spatial resolution of a synthetic aperture radar (SAR) that is extensively used for studies of ocean waves is critically dependent on the so-called scene coherence time of the backscattering Bragg waves on the ocean surface that are in resonance with the incident electromagnetic radar wave [44]. Measurements of coherent properties of those waves using an *L*-band (Bragg wavelengths $\lambda_B \approx 0.24\,\mathrm{m}$) and *X*-band ($\lambda_B \approx 0.03\,\mathrm{m}$) regular and interferometric SAR yielded characteristic scene coherence times of the order of the corresponding Bragg wave periods [45–47]. Note that the range of lengths of the gravity-capillary and short gravity waves in the present study comprises the lengths of the resonant Bragg waves of radars operating in different bands that are used for measurements of waves and currents in the ocean. The coherence times measured directly in this study demonstrate that pure wind waves effectively lose coherence after approximately three periods of the local dominant wave. Figure 10 shows that the duration normalized by the dominant wave period at which the coherence of the wind waves is retained is practically constant. This conclusion is remarkably general, and the loss of coherence within three wave periods was demonstrated for a wide range of wind velocities and fetches.

An additional problem that is closely related to the wave coherence pertains to the randomization of an initially deterministic wave that propagates under the action of steady wind. Figures 11–13 demonstrate that while the pure wind waves lose coherence rapidly and become fully stochastic, in the absence of wind the wavemaker-generated waves remain regular over the whole extent of the test section. The minor loss of coherence may be attributed mainly to weak dissipation at the air-water interface and at solid walls of the tank, as well as to some reflection from the beach at the far end. For wavemaker frequencies, $f_{\mathrm{WM}} > 4\,\mathrm{Hz}$, the presence of wind at all velocities U employed in the present study causes full loss of coherence of the initially regular wave prior to its arrival to the far end of the test section. For lower values of f_{WM} and thus longer deterministic waves, the coherence is not lost completely. Even though the peak of $\mathrm{MSC}(f)$ at $f = f_{\mathrm{WM}}$ is detectable in Figs. 14(a) and 14(b) at low values of U, the spatial coherence of the wind-wave field in the presence of the mechanically generated waves in all panels of that figure is characterized mainly by a pronounced peak at the local dominant frequency. The peaks at f_{WM} grow as the wind velocity increases causing faster augmentation of the dominant wave. When the frequency downshifting results in the wave energy accumulation at frequencies close to f_{WM}, the maximum values of MSC can approach unity; see Fig. 14(c). Note that the wavelength $\lambda(f = 2\,\mathrm{Hz})$ exceeds 40 cm, larger than the distance between the probes $\Delta x = x_2 - x_1$ used to calculate the $\mathrm{MSC}(f)$. The high spatial coherence obtained at $f_{\mathrm{WM}} = 2\,\mathrm{Hz}$ in Fig. 14 thus can be attributed in part to low values of $\Delta x/\lambda$. Note that Fig. 10 demonstrates that also for the stochastic pure wind waves, high temporal coherence is still retained after a single wave period.

V. CONCLUSIONS

Interaction of regular wavemaker-generated waves with stochastic broad-banded waves excited by constant wind forcing is studied here in a moderately sized wind-wave facility. The present results indicate that the effect of a regular wave on the local wind-wave field excited by steady blowing wind remains essential as long as the local dominant frequency of the random wind waves stays below that of the regular wave. At those conditions, the mechanically generated wave grows in amplitude under the action of wind. Wind waves at higher frequencies may be strongly affected by higher harmonics of the wavemaker frequency, generated as free waves by the wavemaker. Once the dominant frequency of the wind waves decreases with fetch and falls below that of the regular wave, the effect of the regular wave on the resulting wavefield gradually vanishes, and the wind wavefield eventually becomes unaffected by the mechanically generated waves. Nonlinear interactions among the deterministic mechanically generated and stochastic wind waves can cause enhancement of frequency downshifting of the spectrum when the frequency of the deterministic wave is somewhat below the local dominant frequency of wind waves. Results of field studies [20,48,49] also suggest

that the presence of swell tends to enhance frequency downshift towards lower frequencies, in agreement with the present laboratory results.

The stochastic nature of wind waves is clearly demonstrated. The present results show that for all fetches and wind velocities employed in the experiments, the pure wind waves retain their temporal coherence for about three periods of the local dominant wave. The presence of the deterministic wave affects the coherence of the wavefield as long as its frequency is below the local dominant wave frequency. The trends observed in the present study clearly indicate that once the local dominant frequency due to the downshifting of the frequency spectrum decreases below the frequency of the deterministic wave, the wave field becomes fully stochastic and the regularizing effect of the deterministic wave on coherence vanishes. The results of the present study thus strongly suggest that once dominant wind waves become sufficiently long and the spectral peak shifts to lower frequencies, the statistical parameters of a wave field that evolves with fetch under steady wind forcing become insensitive to both the amplitude and the spectral shape of high-frequency disturbances that may appear at short fetches.

ACKNOWLEDGMENT

Support of this research by the Israel Science Foundation (Grant No. 508/19) is gratefully acknowledged.

[1] L. Cavaleri, S. Abdalla, A. Benetazzo, L. Bertotti, J. R. Bidlot, Ø Breivik, S. Carniel, R. E. Jensen, J. Portilla-Yandun, W. E. Rogers *et al.*, Wavemodelling in coastal and inner seas, Progr. Oceanogr. **167**, 164 (2018).

[2] D. Liberzon and L. Shemer, Experimental study of the initial stages of wind waves spatial evolution, J. Fluid Mech. **681**, 462 (2011).

[3] A. Zavadsky, A. Benetazzo, and L. Shemer, On the two-dimensional structure short gravity waves in a wind wave tank, Phys. Fluids **29**, 016601 (2017).

[4] L. Shemer, On evolution of young wind-waves in time and space, Atmosphere **10**, 562 (2019).

[5] S. A. Kitaigorodskii, Application of the theory of similarity to the analysis of wind generated wave motion as a stochastic process, Bull. Acad. Sci. USSR, Geophys. Ser. Engl. Transl. **N1**, 73 (1962).

[6] H. Mitsuyasu, On the growth of the spectrum of wind generated waves I, Rep. Res. Inst. Appl. Mech. Kyushu Univ. **16**, 459 (1968).

[7] H. Mitsuyasu and T. Honda, Wind-induced growth of water waves, J. Fluid. Mech. **123**, 425 (1982).

[8] A. Zavadsky, D. Liberzon, and L. Shemer, Statistical analysis of the spatial evolution of the stationary wind wave field, J. Phys. Oceanogr. **43**, 65 (2013).

[9] S. I. Badulin, A.V. Babanin, V. E. Zakharov, and D. Resio, Weakly turbulent laws of wind-wave growth, J. Fluid Mech. **591**, 339 (2007).

[10] V. E. Zakharov, S. I. Badulin, V. V. Geogjaev, and A. N. Pushkarev, Weak-turbulent theory of wind-driven sea, Earth Space Sci. **6**, 540 (2019).

[11] H. Mitsuyasu, Interactions between water waves and wind (I). Rep. Res. Inst. Appl. Mech. Kyushu Univ. **14**, 67 (1966).

[12] O. M. Phillips and M. L. Banner, Wave breaking in the presence of wind drift and swell, J. Fluid Mech. **66**, 625 (1974).

[13] M. Donelan, The effect of swell on the growth of wind waves. Johns Hopkins APL Technical Digest **8**, 18 (1987).

[14] G. Chen and S. E. Belcher, Effects of Long Waves on Wind-Generated Waves., J. Phys. Oceanogr. **30**, 2246 (2000).

[15] T. Bailey, L. Ross, M. Bryant, and D. Bryant, Predicting Wind Wave Suppression on Irregular Long Waves, J. Marine Sci. Eng. **8**, 619 (2020).

[16] T. Waseda and M. P. Tulin, Experimental study of the stability of deep-water wave trains including wind effects, J. Fluid Mech. **401**, 55 (1999).
[17] G. Caulliez, V. Makin, and V. Kudryavtsev, Drag of the water surface at very short fetches: Observations and modeling, J. Phys. Oceanogr. **38**, 2038 (2008).
[18] D. Masson, On the nonlinear coupling between swell and wind waves, J. Phys. Oceanogr. **23**, 1249 (1993).
[19] I. R. Young, Directional spectra of hurricane wind waves, J. Geophys. Res. **111**, C08020 (2006).
[20] C. L. Vincent, H. C. Graber, and C. O. Collins lll, Effect of swell on Wind Stress for Light to Moderate Winds, J. Atmos. Sci. **77**, 3759 (2020).
[21] L. Grare, W. L. Peirson, H. Branger, J. W. Walker, J. P. Giovanangeli, and V. K. Makin, Growth and dissipation of wind-forced, deep water waves, J. Fluid Mech. **722**, 5 (2013).
[22] M. Buckley, F. Veron, and K. Yousefi, Surface viscous stress over wind-driven waves with intermittent airflow separation, J. Fluid Mech. **905**, A31 (2020).
[23] K. Yousefi, F. Veron, and P. Buckley, Momentum flux measurements in the airflow over wind-generated surface wave, J. Fluid Mech. **895**, A15 (2020).
[24] M. Hatori, M. Tokuda, and Y. Toba, Experimental study on strong interaction between regular waves and wind waves, J. Oceanogr. Soc. Jpn. **37**, 111 (1981).
[25] Y. Imai, M. Hatori, M. Tokuda, and Y. Toba, Experimental study on strong interaction between regular waves and wind waves-ii, J. Oceanogr. Soc. Jpn. **28**, 87 (1981).
[26] M. Hatori and Y. Toba, Transition of mechanically generated regular waves to wind waves under the action of wind, J. Fluid Mech. **130**, 397 (1983).
[27] L. Shemer, S. K. Singh, and A. Chernyshova, Spatial evolution of young wind-waves: Numerical modeling verified by experiment, J. Fluid Mech. **901**, A22 (2020).
[28] V. E. Zakharov, Stability of periodic waves of finite amplitude on the surface of deep fluid, J. Appl. Mech. Tech. Phys. **9**, 190 (1968).
[29] A. Zavadsky and L. Shemer, Characterization of turbulent airflow over evolving water-waves in a wind-wave tank, J. Geophys. Res. **117**, C00J19 (2012).
[30] A. Zavadsky and L. Shemer, Measurements of waves in a wind-wave tank under steady and time-varying wind forcing, J. Vis. Exp. **132**, 56480 (2018).
[31] A. Ramamonjiarisoa and M. Coantic, Loi experimentale de dispersion des vagues produites par le vent sur une faible longueur d'action, C. R. Acad. Sci. **282**, 111 (1976).
[32] A. Khait and L. Shemer, Nonlinear wave generation by the wavemaker in deep to intermediate water depth, Ocean Eng. **182**, 222 (2019).
[33] V. P. Krasitskii, On the reduced equations in the Hamiltonian theory of weakly nonlinear surface waves, J. Fluid Mech. **272**, 1 (1994).
[34] M. Stiassnie and L. Shemer, Energy computations for coupled evolution of class I and class II instabilities of stokes waves, J. Fluid Mech. **174**, 299 (1987).
[35] H. A. Schaffer, Second-order wavemaker theory for irregular waves, Ocean Eng. **23**, 47 (1996).
[36] E. Kit, L. Shemer, E. Pelinovsky, T. Talipova, O. Eitan, and H. Jiao, Nonlinear wave group evolution in shallow water, Waterway, Port, Coastal and Ocean Eng. **126**, 221 (2000).
[37] A. Zavadsky and L. Shemer, Water waves excited by near-impulsive wind forcing, J. Fluid Mech. **828**, 459 (2017).
[38] G. Caulliez, G. Ricci, and R. Dupont, The generation of the first visible wind waves, Phys. Fluids **10**, 757 (1998).
[39] A. Zavadsky and L. Shemer, Investigation of statistical parameters of the evolving wind wave field using a laser slope gauge, Phys. Fluids **29**, 056602 (2017).
[40] J. W. Wright, The wind drift and wave breaking, J. Phys. Oceanogr. **6**, 402 (1976).
[41] K. Hasselmann, On the nonlinear energy transfer in gravity wave spectrum part 1, General theory, J. Fluid Mech. **12**, 481 (1962).
[42] O. M. Phillips, On the generation of waves by turbulent wind, J. Fluid Mech. **2**, 417 (1957).
[43] A. V. Slunyaev, Effects of coherent dynamics of stochastic deep-water waves, Phys. Rev. E **101**, 062214 (2020).

[44] K. Hasselmann, R. K. Raney, W. J. Plant, W. Alpers, R. A. Shuchman, D. R. Lyzenga, C. L. Rufenach, and M. J. Tucker, Theory of synthetic aperture radar ocean imaging: A MARSEN view, J. Geophys. Res. **90**, 4659 (1985).

[45] W. Alpers and C. Bruening, On the relative importance of motion-related contributions to the SAR imaging mechanism of ocean surface waves, IEEE Trans. Geosci. Remote Sens. **GE-24**, 873 (1986).

[46] L. Shemer and M. Marom, Estimates of ocean coherence time by an interferometric SAR, Int. J. Remote Sens. **14**, 3021 (1993).

[47] S. Suchandtand and R. Romeiser, X-band sea surface coherence time inferred from bistatic SAR interferometry, IEEE Trans. Geosci. Remote Sens. **55**, 3941 (2017).

[48] P. A. Hwang, H. Garcia-Nava, and F. J. Ocampo-Torres, Observations of wind wave development in mixed seas and unsteady wind forcing, J. Phys. Oceanogr. **41**, 2343 (2011).

[49] M. A. Donelan, W. M. Drennan, and K. B. Katsaros, The air-sea momentum flux in mixed wind sea and swell conditions, J. Phys. Oceanogr. **27**, 2087 (1997).